actuators

MDPI

Article

Effects of the Installation Location of a Dielectric Barrier Discharge Plasma Actuator on the Active Passage Vortex Control of a Turbine Cascade at Low Reynolds Numbers

Takayuki Matsunuma

National Institute of Advanced Industrial Science and Technology (AIST), 1-2-1 Namiki, Tsukuba 305-8564, Japan; t-matsunuma@aist.go.jp

Abstract: Because axial flow turbines are widely used as the main components of jet engines and industrial gas turbines, their energy reduction effect is significant, even with a slight performance improvement. These turbines operate over a wide range of Reynolds numbers. However, at low Reynolds numbers below 1×10^5, the aerodynamic characteristics deteriorate greatly, due to the flow separation of the boundary layer on the blade suction surface and an increase in the secondary flow. In this study, an experiment to reduce the passage vortex was conducted using a dielectric barrier discharge plasma actuator, which is expected to operate with a new innovative active flow control technology. The plasma actuator was installed on the endwall of a linear turbine cascade in the test section of a wind tunnel. From the velocity distribution measured using particle image velocimetry, the secondary flow vector, turbulence intensity, and vorticity were analyzed. The input voltage and frequency of the plasma actuator were fixed at 12 $kV_{p\text{-}p}$ and 10 kHz, respectively. In particular, the optimum installation location of the plasma actuator was examined from upstream to mid-passage positions of the turbine cascade (normalized axial location of $Z/C_{ax} = -0.35$ to 0.51). In addition, the effect of the Reynolds number was examined by varying it between $Re_{out} = 1.8 \times 10^4$ and 3.7×10^4. From the experimental results, it was found that the optimum location of the plasma actuator was immediately before the blade leading edge ($Z/C_{ax} = -0.20$ to -0.06). This is because the inlet boundary layer can be accelerated near the blade leading edge, weakening the horseshoe vortex which initially causes the passage vortex. At a higher Reynolds number, the passage vortex suppression effect of the plasma actuator is weakened, because the flow induced by the plasma actuators becomes relatively weaker as the mainstream velocity increases with an increase in the Reynolds number.

Keywords: plasma actuator; turbine blade; secondary flow; passage vortex; active flow control; particle image velocimetry

Citation: Matsunuma, T. Effects of the Installation Location of a Dielectric Barrier Discharge Plasma Actuator on the Active Passage Vortex Control of a Turbine Cascade at Low Reynolds Numbers. *Actuators* **2022**, *11*, 129. https://doi.org/10.3390/act11050129

Academic Editor: Kenji Uchino

Received: 2 March 2022
Accepted: 29 April 2022
Published: 2 May 2022

1. Introduction

Axial flow turbines, used as the main components of jet engines and power generating gas turbines, are widely used worldwide; research on turbine aerodynamics has been carried out for decades, as even a slight performance improvement has a significant energy-saving effect [1–4]. Turbine blades for aircraft propulsion are designed for peak performance under high-Reynolds-number conditions, such as during takeoff and landing. In general, the turbine blade operates in a high-Reynolds-number range of the order of 10^5 or more, where the entire boundary layer of the blade surface can be considered fully turbulent. However, for a gas turbine in a small aircraft such as an unmanned aerial vehicle operating at a high altitude with a low air density, the Reynolds number at the turbine blades drops from 1×10^4 to 2.5×10^4 [5]. In such a low-Reynolds-number region, the boundary layer on the suction surface develops a laminar and transitional region. It is known that the aerodynamic characteristics of the turbine blade deteriorate significantly as flow separation

from the blade suction surface and secondary flows perpendicular to the freestream flow, such as the passage vortex (described later) and blade tip leakage vortex, are strengthened.

Many studies on the aerodynamics of turbine blade rows in low-Reynolds-number regions have been published [6–13]. Sharma [14] showed an approximately 300% increase in the loss coefficient at Reynolds numbers below 1×10^5 compared with that at higher values.

Conventional turbine blades must possess good aerodynamic characteristics in the low-Reynolds-number region for suppressing flow separation on the blade suction surface and secondary flows; however, this leads to a high possibility of impairing the aerodynamic characteristics at original design points such as during takeoff and landing under high Reynolds numbers.

For this reason, the passive or active control of flow separation and secondary flow in the low-Reynolds-number region is important for improving turbine performance, and many technologies have been proposed so far, as described below.

In flow separation control on the suction surface side of the turbine blade, a vortex generator and dimples [15] have been used as passive control devices, and synthetic jets [16] and plasma actuators [17–23] have been used as active control devices. For controlling tip leakage vortex, winglets [24,25] have been used as passive control devices and blowing jets [26] and plasma actuators [27–29] as active control devices. For controlling passage vortices, non-axisymmetric endwall contouring [30], leading-edge fillets/bulbs [31], a boundary layer endwall fence [32], an undulated blade [33], etc., have been used as passive control devices, and air suction [34], steady jet blowing [35], pulsed jet blowing [36], and plasma actuators [37] have been used as active flow control devices.

Passive control devices such as vortex generators are an effective solution for reducing flow separation and secondary flow, but there is a weak point at which unwanted drag occurs under the high-Reynolds-number condition, which is the original operation point. Even though active control devices can be turned off when not required, giving the advantage of not generating unnecessary drag, these air suction and injection devices impose substantial weight penalties. Moreover, active control devices are technically difficult compared to passive control devices, and further research is necessary for practical applications.

Plasma actuators are attractive alternatives because they operate on a new type of active fluid control technology that has no moving mechanical components and a very-high-frequency response that enables real-time control. In addition, they are simple and cost-effective, with free choice of installation location and the possibility of integration into the design of the wing model. For these reasons, the application of active flow control by plasma actuators is very promising and has been extensively investigated in science and industry for turbomachinery. For compressor blades, research of flow separation reduction [38], blade tip leakage flow reduction [39], surge margin improvement [40] were conducted. For turbine blades, research of flow separation reduction [17–23], blade tip leakage flow reduction [27–29], and passage vortex reduction [37] were conducted.

The purpose of this study was to reduce the passage vortex, which is one of the secondary flows that decrease turbine blade performance, using a plasma actuator installed on the endwall. The passage vortex is a vortex in which the boundary layer upstream of the turbine hits the leading edge of the blade and rolls up to form a horseshoe vortex, which moves to the suction surface side of the adjacent turbine blade and develops while adding a wall boundary layer inside the blade passage. Figure 1 shows an outline of the passage vortex generated in the turbine blade row. In a turbine blade with a large turning angle, the passage vortex loss accounts for 30–50% of the total pressure loss [41]. In the design of the latest turbine blade row, because the number of blades is reduced to give highly loaded blades, the passage vortex tends to be stronger, and its reduction will greatly improve the aerodynamic characteristics of the turbine blade.

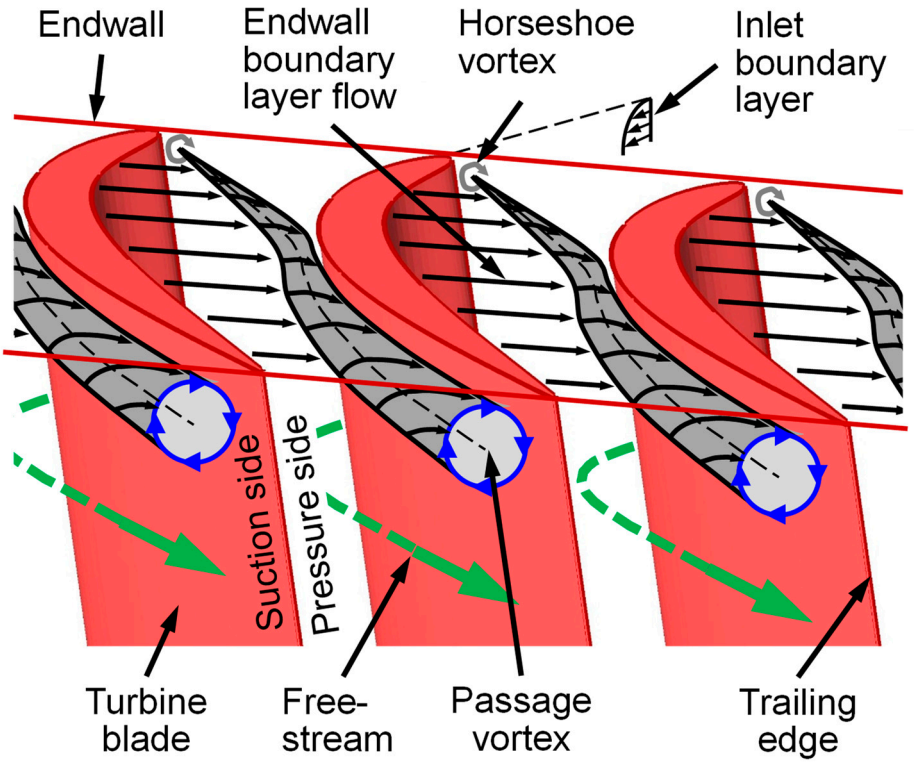

Figure 1. Passage vortex generated in turbine blades.

Figure 2 shows the outline of the plasma actuator. Two electrodes are attached to the top and bottom of the insulation material, and a plasma is generated at the end of the surface top electrode by applying a high-frequency voltage. This plasma induces a one-way flow along the surface. Roth et al. [42] first measured the plasma wall jet induced by a dielectric barrier discharge (DBD) plasma actuator in quiescent air using a pitot probe. Corke et al. [43,44] and Wang et al. [45] recently reviewed DBD plasma actuators.

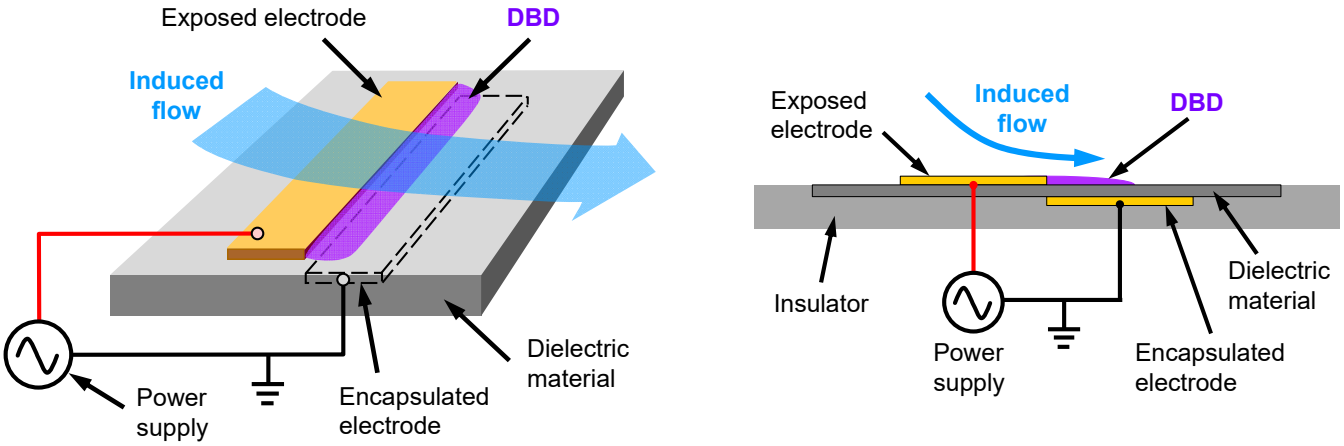

Figure 2. Schematic illustration of the DBD plasma actuator: (**a**) schematic of the plasma actuator; (**b**) cross section.

In this study, the effect of the installation location of a plasma actuator on the active control of the passage vortex of a turbine blade was experimentally investigated using a plasma actuator on the endwall. From the measured velocity distribution obtained by particle image velocimetry (PIV), the secondary flow vector, turbulence intensity, and

vorticity were analyzed. The input voltage of the plasma actuator was fixed at 12 kV_{p-p}, and the input frequency was fixed at 10 kHz. The plasma actuator was located at seven points, from upstream to near the center of the turbine blade (normalized axial locations of $Z/C_{ax} = -0.35$ to 0.51), and the optimum installation location was clarified. The experiment was carried out using two Reynolds numbers, $Re_{out} = 1.8 \times 10^4$ and 3.7×10^4, and the effect of this difference was also examined.

Regarding the installation location of plasma actuators, Huang [20] stated that "the flow control is most effective when it is applied just before the separation point" for the flow separation control of a turbine cascade. In some studies, the plasma actuator was installed just before flow separation [17–19], whereas in others it was installed just after flow separation [21–23]. However, the optimal installation location of the plasma actuator for control of secondary vortices (tip leakage and passage vortices) in turbomachinery has not been investigated. Zhang et al. [39] studied the optimal installation location of the plasma actuators on the tip endwall for compressor tip leakage flow control. They used two plasma actuators and found that plasma actuation at a location at 20% of the chord ($Z/C_{ax} = 0.20$) achieved the optimal flow control effect. However, the optimal installation location of the plasma actuators on the endwall for the turbine passage vortex has not yet been investigated. Therefore, in particular, this study focused on the effect of the installation location of the plasma actuator on the passage vortex control of a turbine cascade.

2. Materials and Methods

2.1. Wind Tunnel and Linear Turbine Cascade

Figure 3 shows the measurement test section of the linear turbine cascade. As shown in Figure 3a, the airflow coming from the blower of the small low-velocity, open-circuit, blowing-type wind tunnel was sent to the test section. A linear turbine cascade with six blades was installed in the test section. The distribution of the secondary flow velocity downstream of the turbine blade was measured using PIV, with a measurement area of 56.1 mm × 44.5 mm. Figure 3b shows the top view of the test section and the blade geometry.

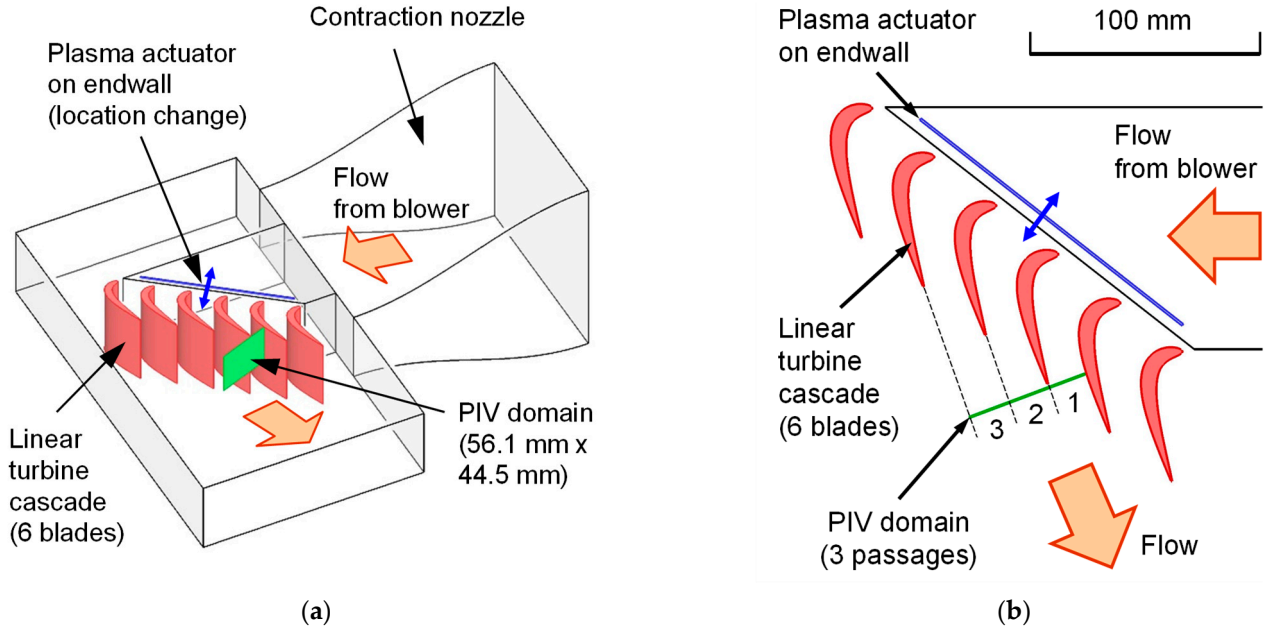

Figure 3. Test section of the linear turbine cascade: (**a**) overall view; (**b**) top view and blade geometry.

Table 1 lists the specifications of the linear turbine cascade. The blade chord length was 58.65 mm, the blade height was 75 mm, and the blade pitch was 35.47 mm. The blade shape was reproduced from the rotor blade hub part of the annular turbine wind tunnel at

AIST [46]. A transparent heat-resistant resin (TSR-884B, CMET Inc., Yokohama, Kanagawa, Japan) was used to manufacture the linear turbine cascade using stereolithography (ATOM m-4000, CMET Inc., Yokohama, Kanagawa, Japan). The forming layer pitch of the machine was set at 100 µm. To reduce the reflection of the laser radiation, the turbine blades were sprayed with matt black paint.

Table 1. Specifications of the linear turbine cascade.

Parameter	Symbol	Value
Number of blades	N	6
Chord length	C	58.65 mm
Axial chord length	C_{ax}	49.43 mm
Blade height	H	75.00 mm
Blade pitch	S	35.47 mm
Inlet flow angle	α_{in}	51.86°
Outlet flow angle	α_{out}	58.74°
Turning angle	$\alpha_{in}+\alpha_{out}$	110.60°
Stagger angle	ξ	33.43°

Figure 4 shows the installation locations of the plasma actuator on the acrylic endwall. The Z-coordinate indicates the direction of the blade axial chord length, and the blade leading edge corresponds to the origin $Z = 0$. As shown in Table 2, the actuator installation location was varied over seven locations from $Z = -17.1$ to 25.4 mm ($Z/C_{ax} = -0.35$ to 0.51, where C_{ax} is the blade axial chord length of 49.43 mm). The flow velocity of the test section was varied by changing the rotational speed of the wind tunnel blower. Table 3 shows the relationship between the rotational speed of the blower and the inlet freestream velocity, outlet freestream velocity, and Reynolds number, based on the outlet freestream velocity and blade chord length of the linear turbine cascade. The inlet and outlet velocities were measured using a pitot pressure probe and hot-wire anemometry. When the rotating speed of the blower was constant, the inlet and outlet velocities were sufficiently stable. Two Reynolds numbers, with low values of approximately 2×10^4 and 4×10^4, were selected for use in this study. It should be noted that this research was conducted under sea-level static pressure conditions (atmospheric pressure, ~101,325 Pa). However, actual gas turbine compressor and turbine stages operate under different pressure conditions. Ashpis and Thurman [47] suggested that the range of pressures where the plasma actuator might be used in gas turbine engines is from 0.03 to 12.4 bar (from 3040 to 1,260,000 Pa in SI units). Valerioti and Corke [48] investigated the pressure dependence of plasma actuators from 0.17 to 9.0 bar (17,200 to 912,000 Pa). They found that the local maximum thrust by the plasma actuator occurred at high pressure (~6 bar). In general, the thrust (and also the velocity) induced by a plasma actuator increases as the ambient pressure increases.

Table 2. Plasma actuator locations.

Location No.	Z (mm)	Z/C_{ax}
1	−17.1	−0.35
2	−10.0	−0.20
3	−2.9	−0.06
4	4.1	0.08
5	11.2	0.23
6	18.3	0.37
7	25.4	0.51

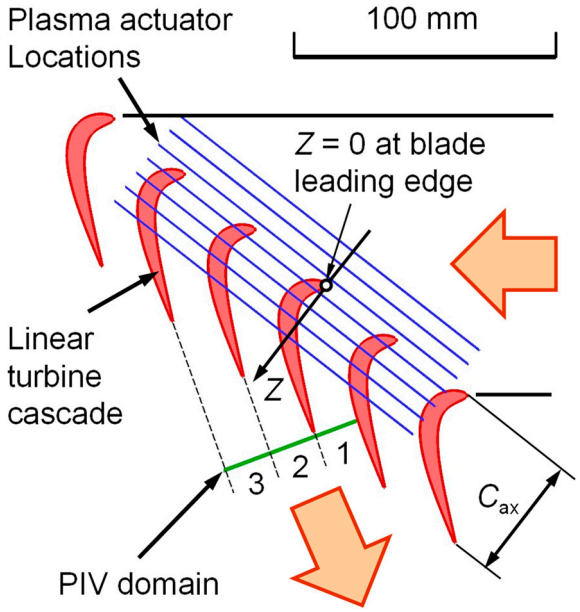

Figure 4. Installation locations of the plasma actuator.

Table 3. Inlet and outlet freestream velocities and Reynolds numbers of the linear turbine cascade.

Rotating Speed of the Blower (Hz)	Inlet Velocity, $U_{FS,in}$ (m/s)	Outlet Velocity, $U_{FS,out}$ (m/s)	Reynolds Number, Re_{out}
225	3.9	4.7	1.8×10^4
450	7.9	9.4	3.7×10^4

2.2. Particle Image Velocimetry Measurements and Data Processing

In this study, PIV was employed to quantify the two-dimensional velocity fields at the outlet of the linear turbine cascade, using a 15 mJ/pulse, double-pulse Nd-YAG laser (NANO S30-15PIV, Litron Laser Ltd., Rugby, Warwickshire, UK). Atomized dioctyl sebacate (DOS) oil with a mean particle diameter of 1 μm was injected upstream of the blower of the wind tunnel via a pressurized oil chamber. Flow image pairs were captured using a camera (PIV CAM 13-8, TSI Inc., Shoreview, MN, USA) with a resolution of 1280 pixels × 1024 pixels and a frame rate of 3.75 Hz. PIV software (Insight Ver. 3.53, TSI Inc., Shoreview, MN, USA) was used for calculating the velocity vectors from the peak correlation of groups of particles between frames, using conventional cross-correlation algorithms on a grid of size 32 × 32 pixels. Three hundred instantaneous velocity pairs were used via PIV to analyze the time-averaged velocity distributions. The number of PIV image pairs (300 pairs) was limited by the capacity of the random access memory (RAM) of the computer used. The measurement time for 300 image pairs was 80 s (=300 pairs/3.75 Hz), and the storage time from RAM to a hard disk was approximately 90 s. Therefore, the PIV measurement time per parameter was approximately 3 min.

The turbulence intensity was calculated as follows:

$$Tu\ [\%] = 100 \times \left(\sqrt{\frac{u_X{}' + u_Y{}'}{2}} \right) / U_{FS,out} \quad (1)$$

where $u_X{}'$ and $u_Y{}'$ are the random velocity fluctuation components in the horizontal (X-coordinate) and vertical (Y-coordinate) directions, respectively.

The velocity and turbulence intensity were nondimensionalized by the freestream velocity at the turbine outlet, with $U_{FS,out}$ values of 4.7 m/s at $Re_{out} = 1.8 \times 10^4$ and 9.4 m/s at $Re_{out} = 3.7 \times 10^4$.

The vorticity component, Ω_{XY}, was calculated as follows:

$$\Omega_{XY}\,[1/\mathrm{s}] = \frac{\partial U_Y}{\partial X} - \frac{\partial U_X}{\partial Y}, \tag{2}$$

where U_X and U_Y are the horizontal (X-coordinate) and vertical (Y-coordinate) velocity components, respectively.

2.3. Plasma Actuator

Figure 5 shows the top and bottom views and cross-sectional schematic of the DBD plasma actuator (A-A′ plane), along with its geometrical dimensions [37]. The plasma actuator used was fabricated using a printed circuit board. The exposed (top) and encapsulated (bottom) electrodes were designed using AutoCAD (Autodesk Inc., San Rafael, CA, USA) and formed by etching a double-sided copper-clad laminate with a dielectric barrier layer made of silicone resin (CS-3975A, Risho Kogyo Co., Ltd., Osaka, Japan). The thicknesses of the top and bottom copper electrodes and the silicone resin dielectric barrier board were 0.018 and 0.44 mm, respectively. The spanwise width of the electrodes was set to L = 150 mm. The streamwise lengths of the top and bottom electrodes were 5 and 15 mm, respectively. As shown on the right of Figure 5, the electrodes were arranged asymmetrically in the streamwise direction, overlapping by 0.5 mm to generate a uniform DBD plasma near one edge of the side of the exposed top electrode.

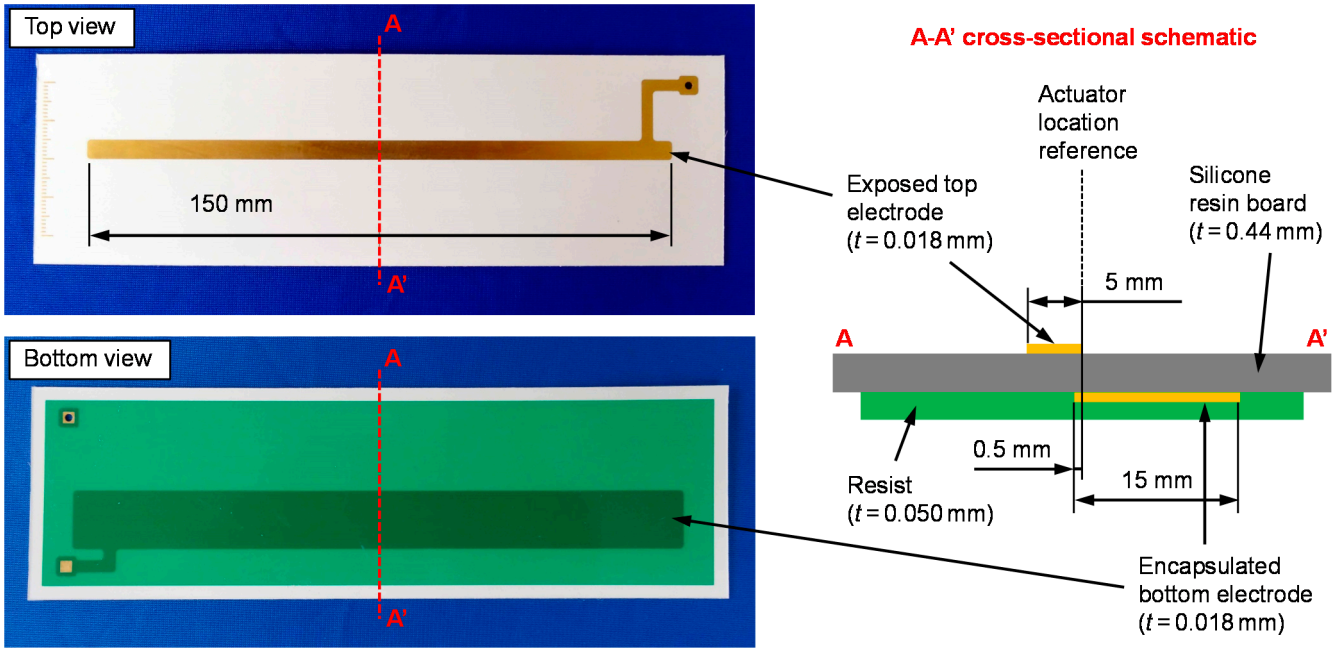

Figure 5. Photographs of the top and bottom views (**left**) and cross-sectional schematic (**right**) of the plasma actuator.

The plasma actuator was excited with a sinusoidal waveform from a high-voltage power amplifier (HAPS-10B40, Matsusada Precision, Inc., Kusatsu, Shiga, Japan). The amplitude of the peak-to-peak input voltage of the plasma actuator was fixed at 12 $\mathrm{kV_{p\text{-}p}}$, and the input voltage frequency was fixed at 10 kHz. These setting values of 12 $\mathrm{kV_{p\text{-}p}}$ and 10 kHz were decided by considering the stability limit of the power supply and the electric strength of the plasma actuator used. The maximum absolute velocity induced by the plasma actuator U_{PA} was approximately 3.8 m/s, and the power consumption P_{PA}/L was approximately 150 W/m.

3. Experimental Results and Discussion

Figure 6 shows an enlarged cross-sectional view of the location of the PIV measurements, as shown in Figure 3a. Three passages of the linear turbine cascade were measured. Passage 1 was located inside the blade, passage 2 at the blade exit, and passage 3 downstream of the blade.

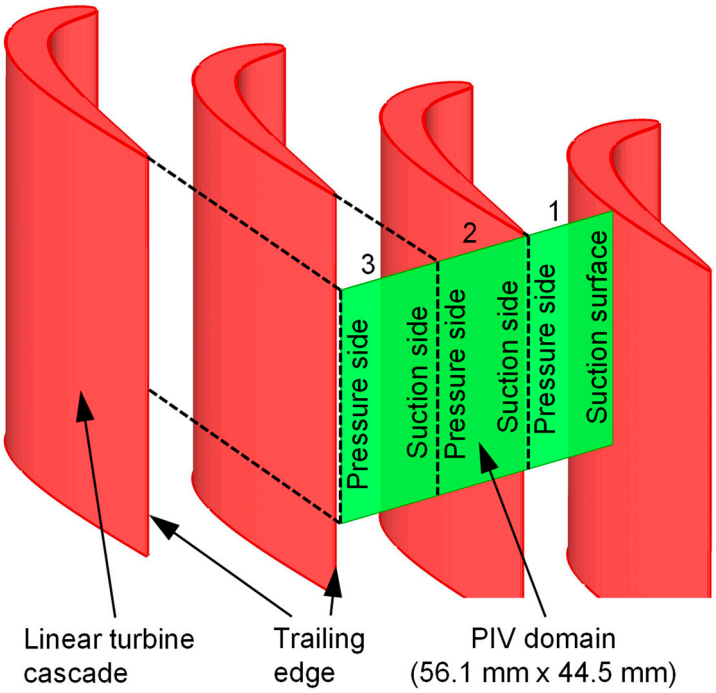

Figure 6. PIV measurement locations.

3.1. Reynolds Number, $Re_{out} = 1.8 \times 10^4$

Figure 7 shows the measured absolute velocity distribution of the secondary flow when the installation location of the plasma actuator was changed. This velocity distribution was nondimensionalized by the freestream velocity of the blade outlet. The peak values of the absolute velocities are shown in the figure.

Figure 7a shows the measurement results under the condition with no control, which forms the baseline. There is a clockwise passage vortex (indicated as PV in the figure) between each blade, and the secondary flow becomes particularly strong when it hits the blade suction surface side.

Figure 7b–h show the measurement results when the plasma actuator is operated. The plasma actuator installed in the endwall is moved from upstream to the inside of the blade. In comparison with Figure 7a, the passage vortex is weakened at this point. When the plasma actuator is operated upstream of the blade leading edge, as shown in Figure 7b–d, it has almost the same absolute velocity distribution. When it is operated inside the blade (Figure 7e–h), the velocity distribution of the secondary flow increases as the installation location moves downstream, and the effect of the passage vortex suppression gradually decreases. In addition, a counterclockwise corner vortex (CV) is generated at the corner of the blade pressure side and endwall, as shown in Figure 7f. This CV is unwanted and appears to be generated by the flow induced by the plasma actuator blowing up to the blade pressure surface side.

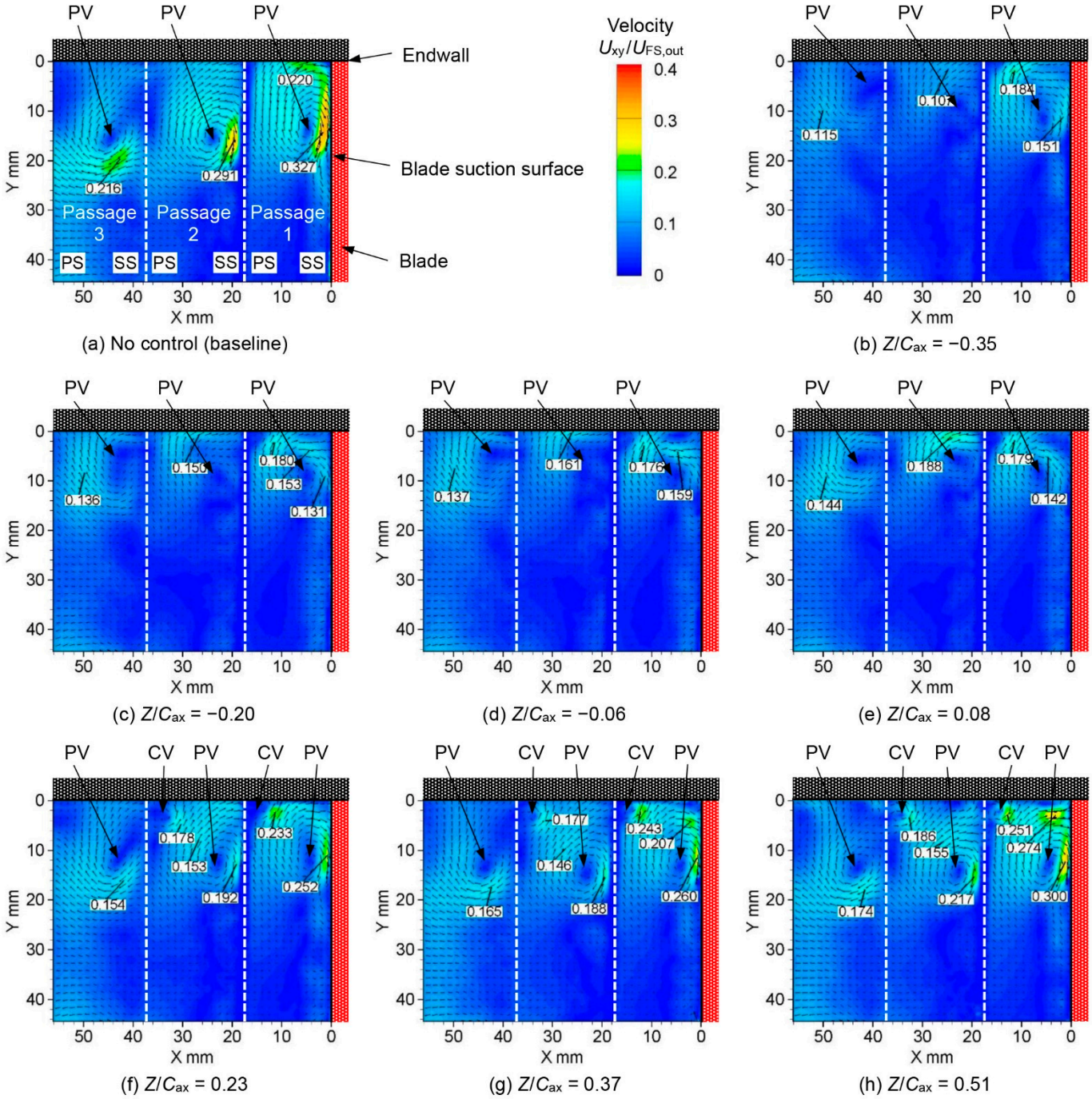

Figure 7. Velocity distributions of secondary flow at the outlet of the linear turbine cascade at various plasma actuator locations ($Re_{out} = 1.8 \times 10^4$).

For a more quantitative understanding, Figure 8 shows the maximum secondary velocity due to the passage vortices for the three blade passages. The black dashed line shows the result with no control (baseline), and the solid red line shows that with flow control. As shown in Figure 8a, in passage 1, inside the blade, when the plasma actuator is installed upstream at Z/C_{ax} = 0.08 near the blade leading edge, the peak velocity is almost constant, and a decrease in the maximum velocity of 46% is observed compared with the no-control condition. In contrast, when the installation is furthest downstream at Z/C_{ax} = 0.51 near the blade mid-chord, the maximum velocity decreases because the controlling effect of the plasma actuator remaines at 8%. As shown in Figure 8b, in passage 2 at the blade exit, a more upstream installation location of the plasma actuator resultes in a lower secondary

flow velocity. When installed at $Z/C_{ax} = -0.35$ (furthest upstream), the maximum velocity decreases by as much as 63%. However, at the furthest downstream location, $Z/C_{ax} = 0.51$, it decreases by only 25%. As shown in Figure 8c, a higher upstream installation location of the plasma actuator results in a lower velocity of the secondary flow. The maximum velocity was reduced by 47% at the furthest upstream location of $Z/C_{ax} = 0.35$ and by only 19% at the furthest downstream location of $Z/C_{ax} = 0.51$.

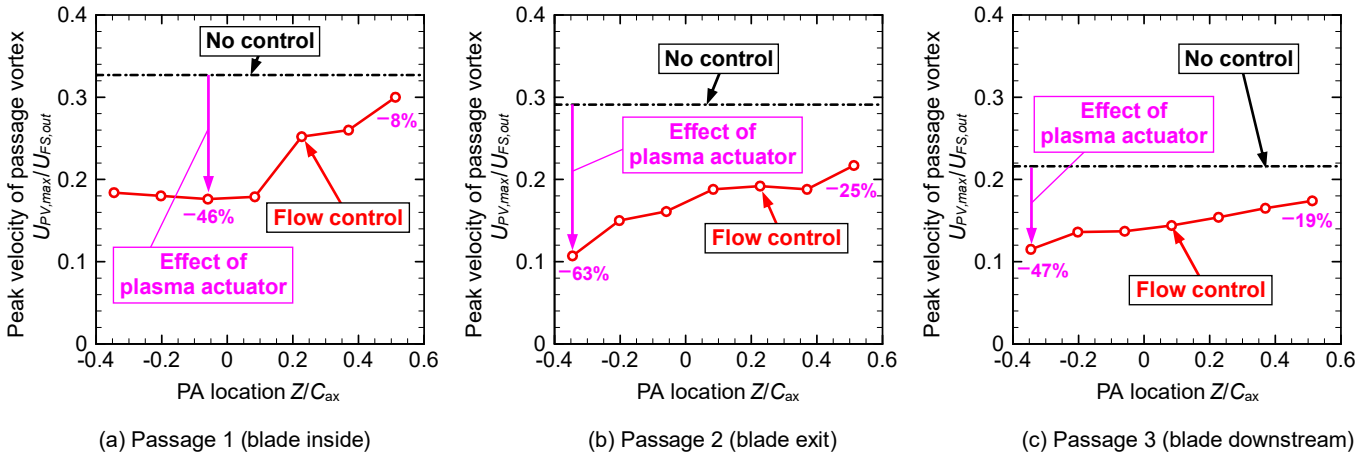

Figure 8. Effect of the plasma actuator location on peak secondary velocity of passage vortex ($Re_{out} = 1.8 \times 10^4$).

Figure 9 shows the streamlines of the secondary flow at each plasma actuator location. Figure 9a shows the streamlines of the secondary flow with no control. A large passage vortex exists in both passages, whose center maintains the spanwise location at Y = approximately 15 mm.

Figure 9b–h show the streamlines of the secondary flow with flow control. When Figure 9a,b are compared, Figure 9b indicates that the center location of the passage vortex approaches the upper endwall surface ($Y = 0$) as the passage vortex moves downstream from passage 1 to passage 3. This indicates that the passage vortex is weakening. Similarly, from Figure 9c–e, the vortex center approaches the endwall surface as it moves downstream from passage 1 to passage 3. However, the effect of the weakening of the passage vortex decreases after Figure 9f. The counterclockwise CV generated at the corner of the blade pressure surface and endwall is observed clearly in the streamlines of the secondary flow in Figure 9f–h.

Figure 10 shows a plot of the center location of the passage vortex at each plasma actuator location in Figure 9. The vortex centers for no control, indicated by the black circles, move in the upper endwall direction with control. When passages 1, 2, and 3 are compared, it can be seen that the movement of the center of the passage vortex in the upper endwall direction increases as it moves downstream.

Figure 11 shows the vertical Y-direction location of the center of the passage vortex in Figure 10 at each plasma actuator location. As shown in Figure 11a, in passage 1, inside the blade, the effect of plasma actuation is significant at $Z/C_{ax} = -0.20$–0.08, and the Y-direction location of the passage vortex center moves by up to 39% towards the upper endwall side. However, the effect is small at $Z/C_{ax} = 0.23$–0.51, and the movement of the vortex center in the Y-direction remains at only 5%. In passage 2, at the blade exit, shown in Figure 11b, this feature of passage 1 becomes remarkable, and the effect is significant when the actuator is installed at the upstream side. At $Z/C_{ax} = 0.08$ especially, the movement towards the endwall is as much as 63%. However, the effect is not as significant downstream at $Z/C_{ax} = 0.23$–0.51, where only a 5% movement is observed at $Z/C_{ax} = 0.37$. In passage 3, downstream of the blade, as shown in Figure 11c, the effect is significant when the location is on the upstream side, and the movement of the vortex center to the upper endwall side

reaches 71% at $Z/C_{ax} = -0.06$. However, downstream after $Z/C_{ax} = 0.23$, the movement decreases rapidly and is only 12% at $Z/C_{ax} = 0.51$.

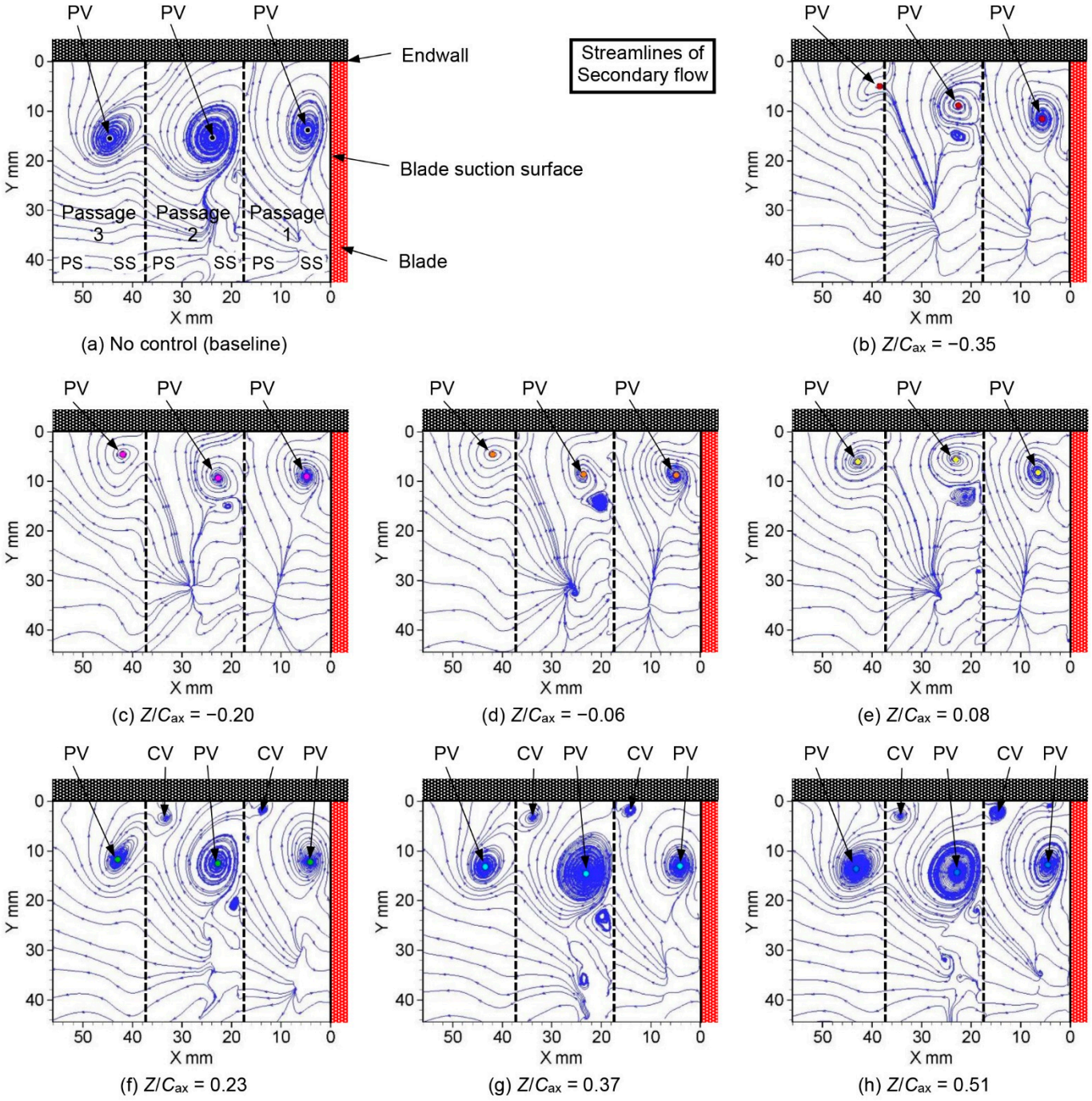

Figure 9. Streamlines of secondary flow at the outlet of the linear turbine cascade at various plasma actuator locations ($Re_{out} = 1.8 \times 10^4$).

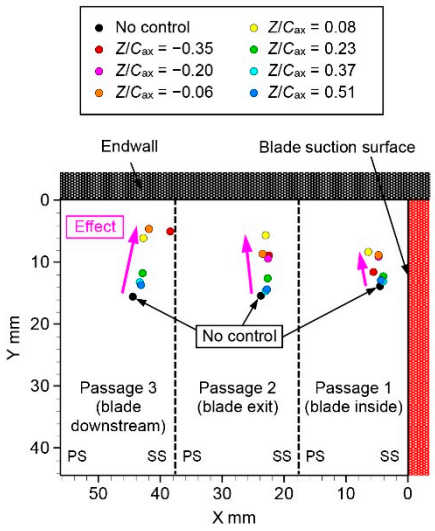

Figure 10. Center positions of passage vortex at various plasma actuator locations ($Re_{out} = 1.8 \times 10^4$).

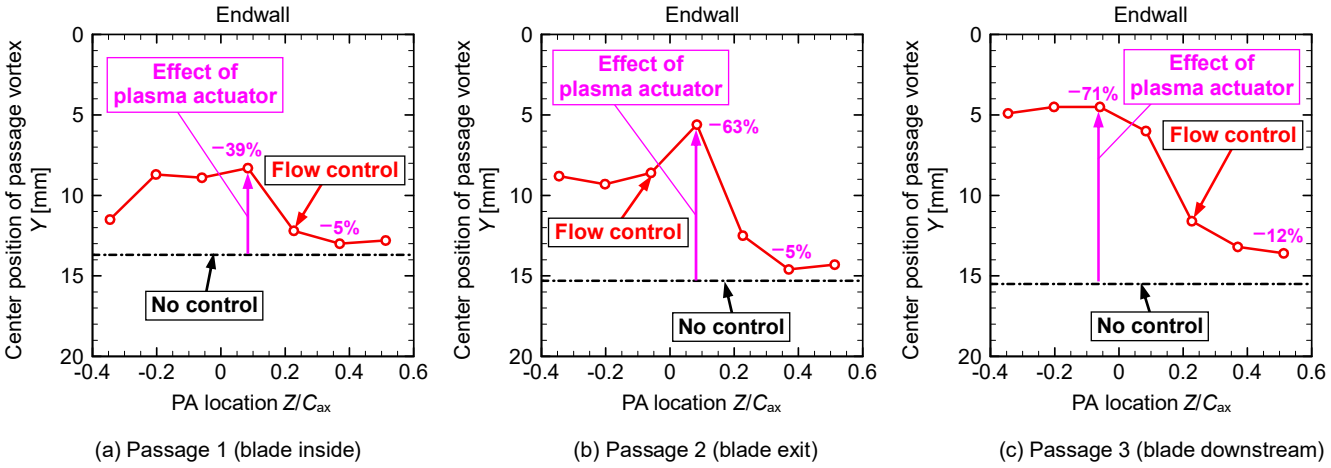

Figure 11. Effect of the plasma actuator location on the center position of the passage vortex ($Re_{out} = 1.8 \times 10^4$).

Figure 12 shows the distribution of turbulence intensities at each actuator location.

Figure 12a shows the distribution of turbulence intensity with no control (baseline). In all three passages, the turbulence intensity is high near the center of the passage vortex, and the peak of the turbulence intensity gradually weakens as it moves downstream from passage 1 to passage 3. In passage 1, inside the blade, a region with a high turbulence intensity of up to 16.4% exists on the blade suction surface, from the center to approximately $Y = 30$ mm, where the flow separation of the boundary layer occurs on the blade suction surface side. The width of separation in the X-direction is large and occupies approximately one third of the blade pitch, due to the low-Reynolds-number condition.

Figure 12b–h show the measurement results with plasma actuation. Comparing Figure 12a,b, the peak of the turbulence intensity at the center of the passage vortex presented in Figure 12a with no control disappears in Figure 12b with flow control. Similarly, from Figure 12c–h, the turbulence intensity peak at the center of the passage vortex is not observed. In Figure 12c–e, where the turbulence intensity in the passage vortex has remarkably disappeared, the region with high turbulence intensity on the blade suction side in passage 1 extends upward to approximately $Y = 20$ mm. This indicates that the flow separation region on the blade suction surface increases in the blade span direction as the passage vortex is weakened. In addition, at more downstream locations, Figure 12f–h show that the turbulence intensity tends to increase because the suppression effect of the passage

vortex weakens. In addition, the counterclockwise CV at the blade pressure surface and endwall generates a high-turbulence-intensity region. The maximum turbulence intensity of the CV is 10%, as shown in Figure 12h.

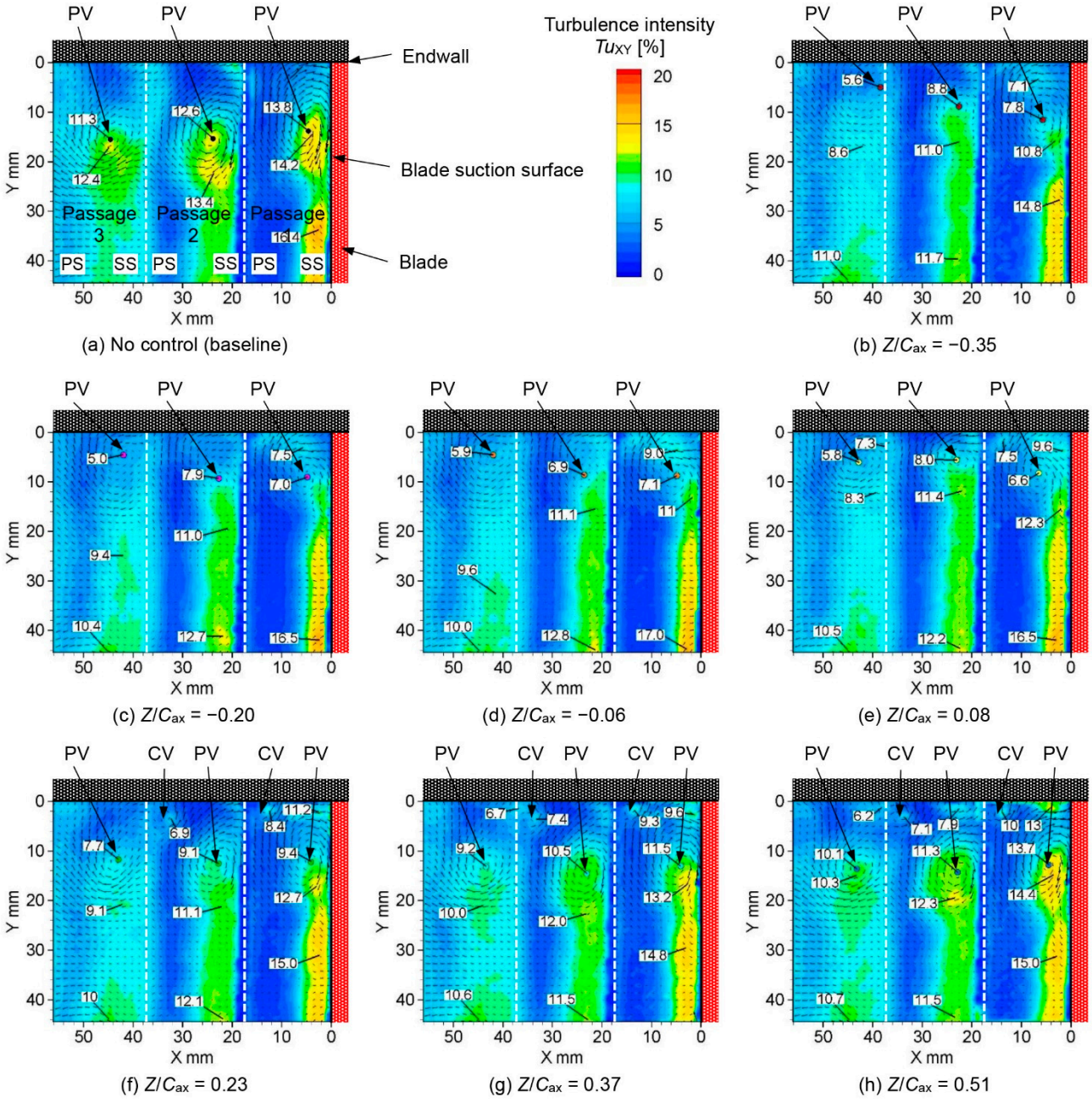

Figure 12. Turbulence intensity distributions of secondary flow at the outlet of the linear turbine cascade at various plasma actuator locations ($Re_{out} = 1.8 \times 10^4$).

Figure 13 shows how the turbulence intensity at the center of the passage vortex of Figure 12 varies according to the plasma actuator location. In passage 1, inside the blade, shown in Figure 13a, the effect is significant from $Z/C_{ax} = -0.35$ to 0.08, and the turbulence intensity is almost halved. In contrast, after $Z/C_{ax} = 0.08$, the turbulence intensity gradually increases, and at $Z/C_{ax} = 0.51$ (13.7%) it is almost the same as that for no control (13.8%). In passage 2, at the blade exit, shown in Figure 13b, a turbulence intensity reduction effect of 45% is observed at $Z/C_{ax} = 0.06$, and the effect is weakened. At the furthest downstream position of $Z/C_{ax} = 0.51$, the reduction effect is only 10%. In passage 3, downstream of the

blade, shown in Figure 13c, the turbulence intensity at the installation location upstream of $Z/C_{ax} = 0.08$ is almost constant, and that at $Z/C_{ax} = -0.20$ is decreased by 56%. However, downstream after $Z/C_{ax} = 0.08$, the reduction effect of turbulence intensity gradually weakens, and that at $Z/C_{ax} = 0.51$ is only 11%.

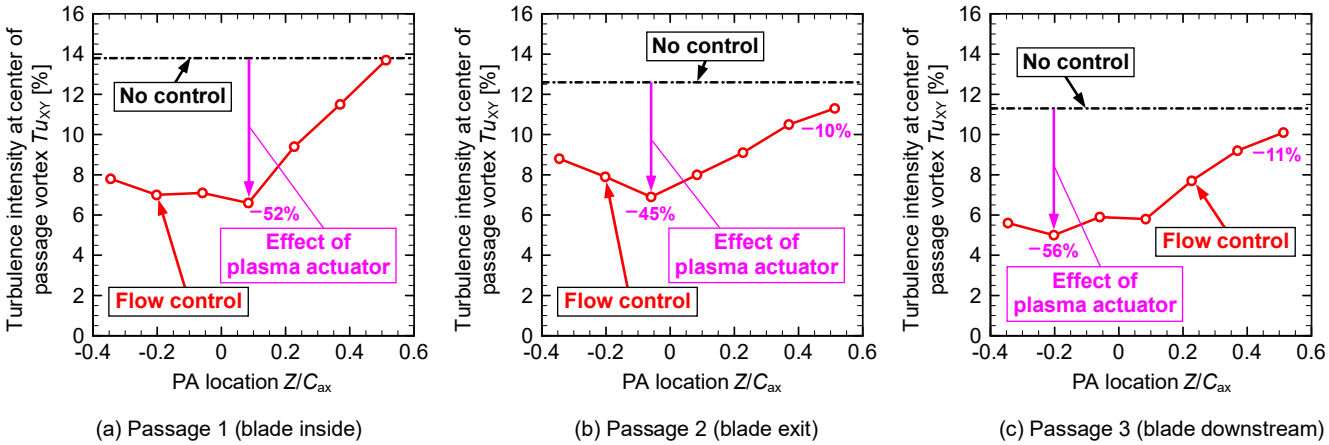

Figure 13. Effect of the plasma actuator location on turbulence intensity at the center of the passage vortex ($Re_{out} = 1.8 \times 10^4$).

Figure 14 shows the vorticity distribution at each plasma actuator location.

Figure 14a shows the vorticity distribution with no control. Because the vorticity defines counterclockwise rotation as positive, the clockwise passage vortex is indicated by a negative value (green to blue in the contour plot). In both passages, the absolute value of the vortex is high near the center of the passage vortex, and the peak of the turbulence intensity gradually weakens downstream from passage 1 to passage 3, with values of −800, −660, and −540 s^{-1}, respectively.

Figure 14b–h show the measurement results when the plasma actuator is operated. Comparing Figure 14a,b, the peak of the vorticity at the center of the passage vortex that exists in Figure 14a with no control is weakened in Figure 14b with flow control. Similarly, from Figure 14c–e, the vorticity of the center of the passage vortex is weakened. However, in Figure 14f–h, which are further downstream, the peak of the vorticity becomes stronger, and the vorticity distribution tends to approach that in Figure 14a with no control, because the suppression effect of the passage vortex weakens. Moreover, a counterclockwise CV with highly positive vorticity is generated at the corner of the pressure surface side (PS) and endwall, i.e., the opposite location to the suction surface side (SS) with passage vortex generation. Although the size of this vortex is small, its peak value is 1580 s^{-1} in passage 1 at $Z/C_{ax} = 0.51$ (the furthest downstream), which is more than twice the value of −720 s^{-1} for the passage vortex.

Figure 15 shows how the vorticity at the center of the passage vortex in Figure 14 changes depending on the plasma actuator location. In passage 1, inside the blade, shown in Figure 15a, the effect of decreasing the absolute value of the vorticity is highest at $Z/C_{ax} = -0.06$, and the vorticity at the center of the passage vortex is reduced by 59%. In contrast, after $Z/C_{ax} = -0.06$, the absolute value of the vorticity gradually increases, and at $Z/C_{ax} = 0.51$ it decreases by only 17% compared to the no-control condition. In passage 2, at the blade exit, shown in Figure 15b, it tends to be like Figure 15a. The most effective location is $Z/C_{ax} = -0.06$, and the vorticity at the center of the passage vortex is weakened by as much as 71%. Furthermore, after $Z/C_{ax} = -0.06$, the absolute vorticity gradually increases, and the furthest downstream position of $Z/C_{ax} = 0.51$ shows a 31% decrease. In passage 3, downstream of the blade, shown in Figure 15c, the effect of decreasing the absolute value of the vorticity is greater as the plasma actuator location is moved further upstream, and a decrease of 80% is observed at the furthest upstream position of $Z/C_{ax} = -0.35$. However,

as the installation location travels further downstream, the vorticity reduction decreases gradually. At the furthest downstream position of Z/C_{ax} = 0.51, the decrease is only 16%.

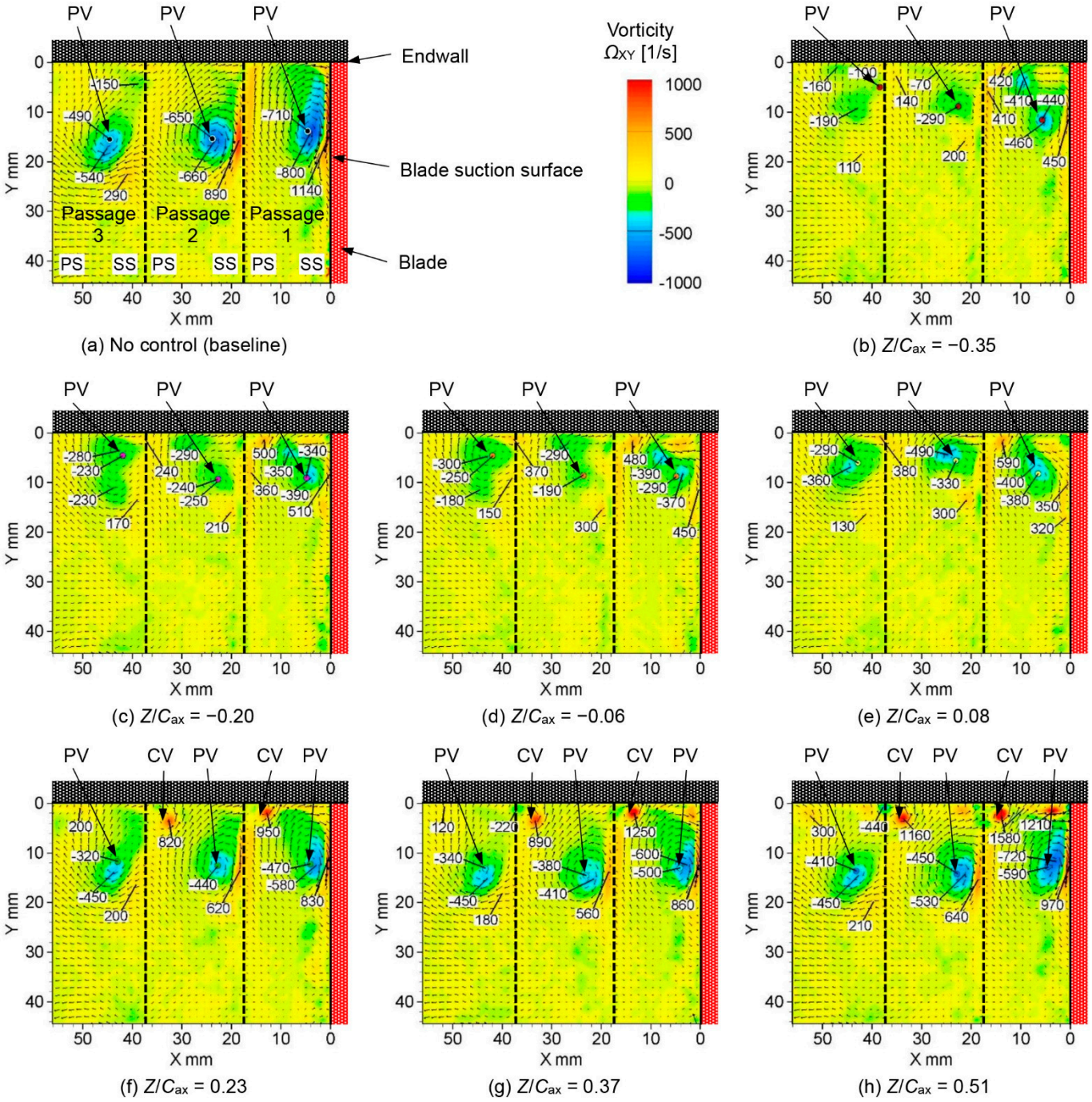

Figure 14. Vorticity distributions of secondary flow at the outlet of the linear turbine cascade at various plasma actuator locations ($Re_{out} = 1.8 \times 10^4$).

Figure 16 shows how the peak value of the negative (clockwise) vorticity in Figure 14 changes with the actuator location. In passage 1, inside the blade, shown in Figure 16a, in the range of Z/C_{ax} = −0.35–0.08, the effect of suppressing the peak value of the vorticity is almost constant. At Z/C_{ax} = −0.20, the absolute value of the vorticity is decreased by 51%, which is almost half of that for no control. However, after Z/C_{ax} = 0.08, the absolute value of the vorticity gradually increases, and at the furthest downstream position at Z/C_{ax} = 0.51, it shows only a 26% decrease compared to no control. In passage 2, at the blade exit, shown

in Figure 16b, it tends to be the same as in Figure 16a. At $Z/C_{ax} = -0.35$ to -0.06, the vorticity peak value has a high suppression effect, and that at $Z/C_{ax} = -0.20$ shows a 62% decrease. At $Z/C_{ax} = 0.08$ or after, the absolute peak value of the vorticity increases, and that at the furthest downstream position of $Z/C_{ax} = 0.51$ shows a decrease of 32%. In passage 3, downstream of the blade, shown in Figure 16c, the decrease in the absolute value of the vorticity increases as the installation location moves further upstream, and a decrease of 65% is observed at the furthest upstream position of $Z/C_{ax} = -0.35$. However, as the installation location moves downstream, the reduction in vorticity is gradually lessened. In addition, after $Z/C_{ax} = 0.23$, the vorticity is almost constant, with a decrease of only 17%.

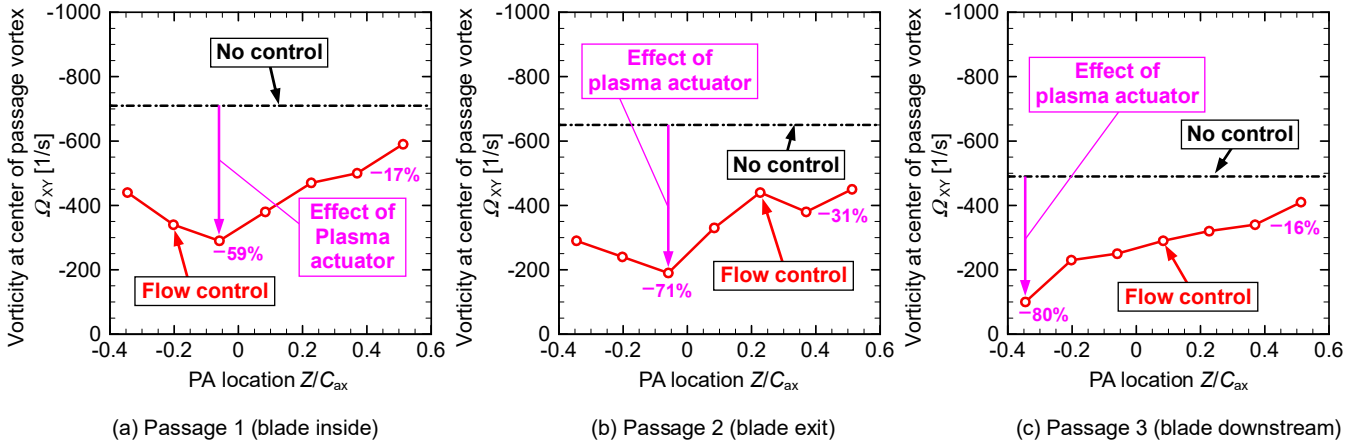

Figure 15. Effect of the plasma actuator location on the vorticity at the center of the passage vortex ($Re_{out} = 1.8 \times 10^4$).

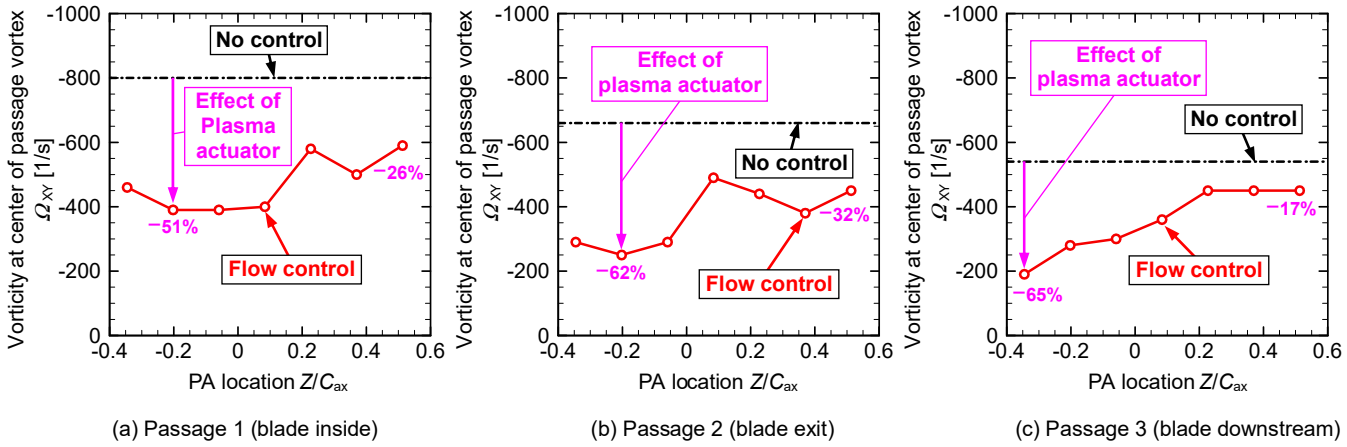

Figure 16. Effect of the plasma actuator location on the peak vorticity of the passage vortex ($Re_{out} = 1.8 \times 10^4$).

In summary, for all the peak values of the velocity distribution, the center location of the passage vortex, the turbulence intensity and vorticity at the center location of the passage vortex, and the negative peak values of the vorticity distributions, the effect was high when the plasma actuator was located further upstream than the blade leading edge, and each value was reduced to less than half. However, as the location moved downstream from the blade leading edge, the effect became weaker.

3.2. Reynolds Number, $Re_{out} = 3.7 \times 10^4$

Figure 17 shows the measured absolute velocity distribution of the secondary flow for the different plasma actuator locations.

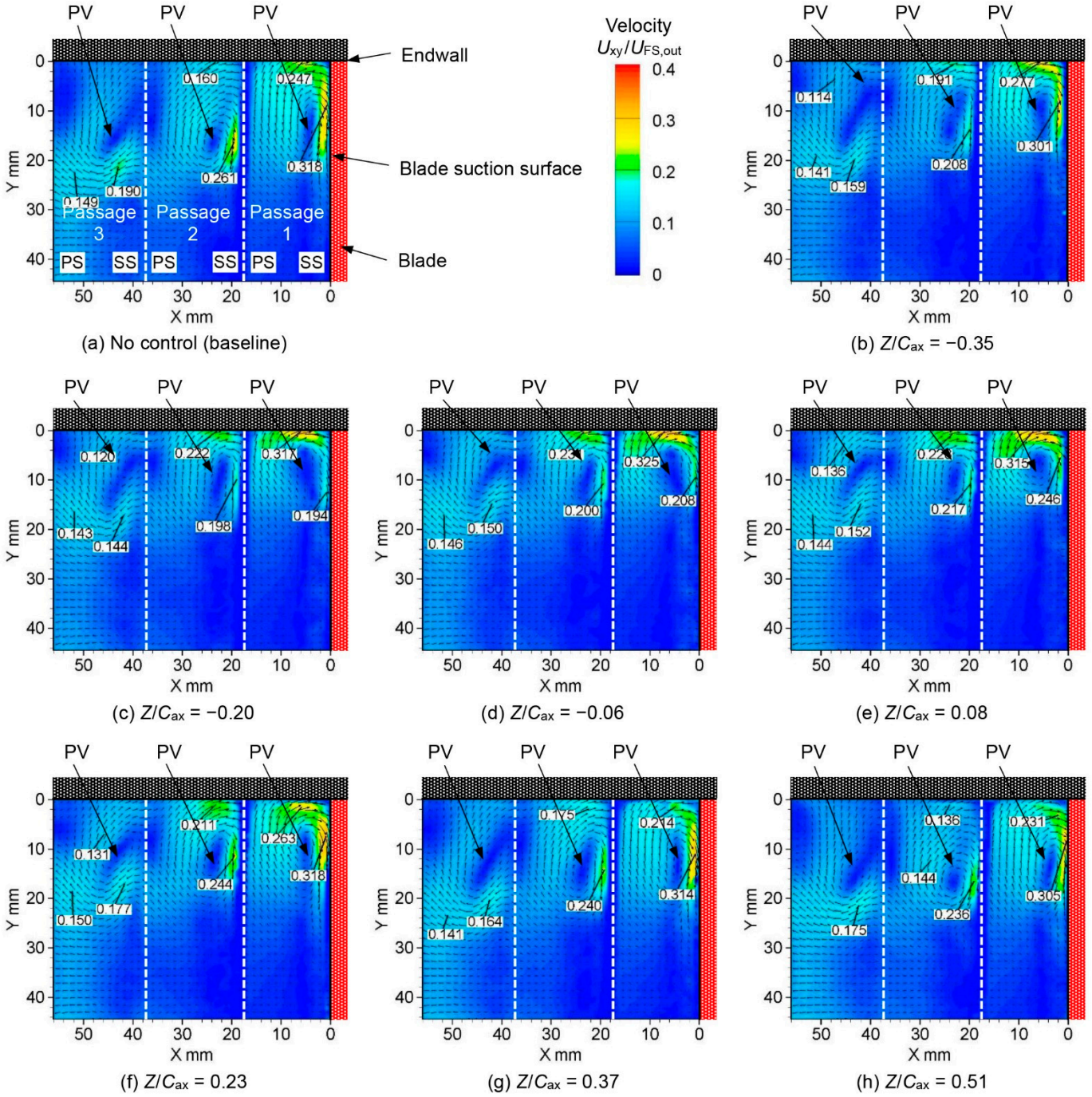

Figure 17. Velocity distributions of secondary flow at the outlet of the linear turbine cascade at various plasma actuator locations ($Re_{out} = 3.7 \times 10^4$).

Figure 17a shows the measurement results with no control, which form the baseline. Compared to the secondary flow velocity distribution at $Re_{out} = 1.8 \times 10^4$ in Figure 7a, the maximum velocity between each blade is weakened, and the secondary flow is also relatively weakened as the Reynolds number increases.

Figure 17b–h show the measurement results when the plasma actuator is operated. Compared to Figure 17a, the passage vortex is weakened. However, overall, the effect of the plasma actuator is less than at the lower Reynolds number of 1.8×10^4.

Figure 18 shows the maximum secondary velocities due to the passage vortices for the three blade passages. As shown in Figure 18a, in passage 1, the effect of the plasma actuator operation is low, and the velocity peak value of the secondary flow generated by

the passage vortex is not significantly different from the case with no control. A decrease of only 5% is observed at the furthest upstream position of $Z/C_{ax} = -0.35$. In passage 2, shown in Figure 18b, the effect of flow control by the plasma actuator is greater than for passage 1, inside the blade (Figure 18a). When the actuator is installed upstream at $Z/C_{ax} = -0.35$, the maximum velocity is reduced by 20%. After $Z/C_{ax} = 0.08$, the peak velocity is almost constant and is decreased by only 7% at $Z/C_{ax} = 0.23$. In passage 3, shown in Figure 18c, a tendency similar to that shown in Figure 18b for the blade exit is observed. Before $Z/C_{ax} = 0.08$, the velocity peak value decreases by 24%, whereas after $Z/C_{ax} = 0.08$, it decreases by only 7%.

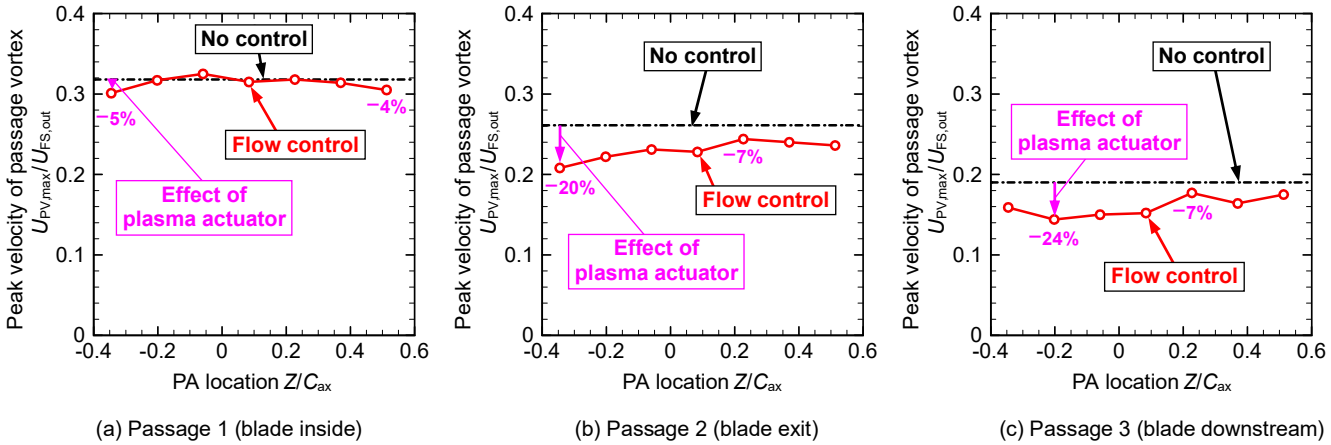

Figure 18. Effect of the plasma actuator location on peak secondary velocity of passage vortex ($Re_{out} = 3.7 \times 10^4$).

Figure 19 shows the results for the streamlines of the secondary flow at each plasma actuator location.

Figure 19a shows the secondary flow with no control. Large passage vortices exist in both passages, and the spanwise (Y-coordinate) direction locations of the center of the passage vortex are approximately $Y = 12$ mm in passage 1, $Y = 16$ mm in passage 2, and $Y = 15$ mm in passage 3.

Figure 19b–h show the measurement results when the plasma actuator is operated. When Figure 19a,b are compared, the center location of the passage vortex approaches the upper side of the endwall surface ($Y = 0$) in Figure 19b. Similarly, Figure 19c–e show that the vortex center approaches the upper endwall surface in all passages. However, in Figure 19f–h, the further downstream the plasma actuator is located, the less weakening occurs in the passage vortex.

Figure 20 shows the center location of the passage vortex at each plasma actuator installation location in Figure 19. The vortex center location for no control, shown by a black circle, moves in the upper endwall direction due to the control by the plasma actuator.

Figure 21 shows how the vertical direction (Y-coordinate) location at the center location of the passage vortex in Figure 20 changes, depending on the plasma actuator installation location. In passage 1, shown in Figure 21a, and in passage 2, shown in Figure 21b, the most effective location is near the blade leading edge, and at $Z/C_{ax} = -0.06$, the Y-direction location of the vortex center moves upward by 59% for passage 1 and 48% for passage 2. The movement of the vortex center in the Y-direction decreases as the plasma actuator is located further away from the blade leading edge, on both the upstream and downstream sides. On the downstream side especially, the center location of the passage vortex at $Z/C_{ax} = -0.51$ is almost the same as the result for no control. In passage 3, shown in Figure 21c, when the installation location is further upstream than $Z/C_{ax} = 0.08$, immediately after the blade leading edge, the center location of the passage vortex remains almost constant, and its movement towards the upper endwall side reaches 59% at $Z/C_{ax} = -0.20$. However, at

positions downstream of Z/C_{ax} = 0.08, the amount of movement gradually decreases, and the position of the passage vortex becomes the same as that for no control.

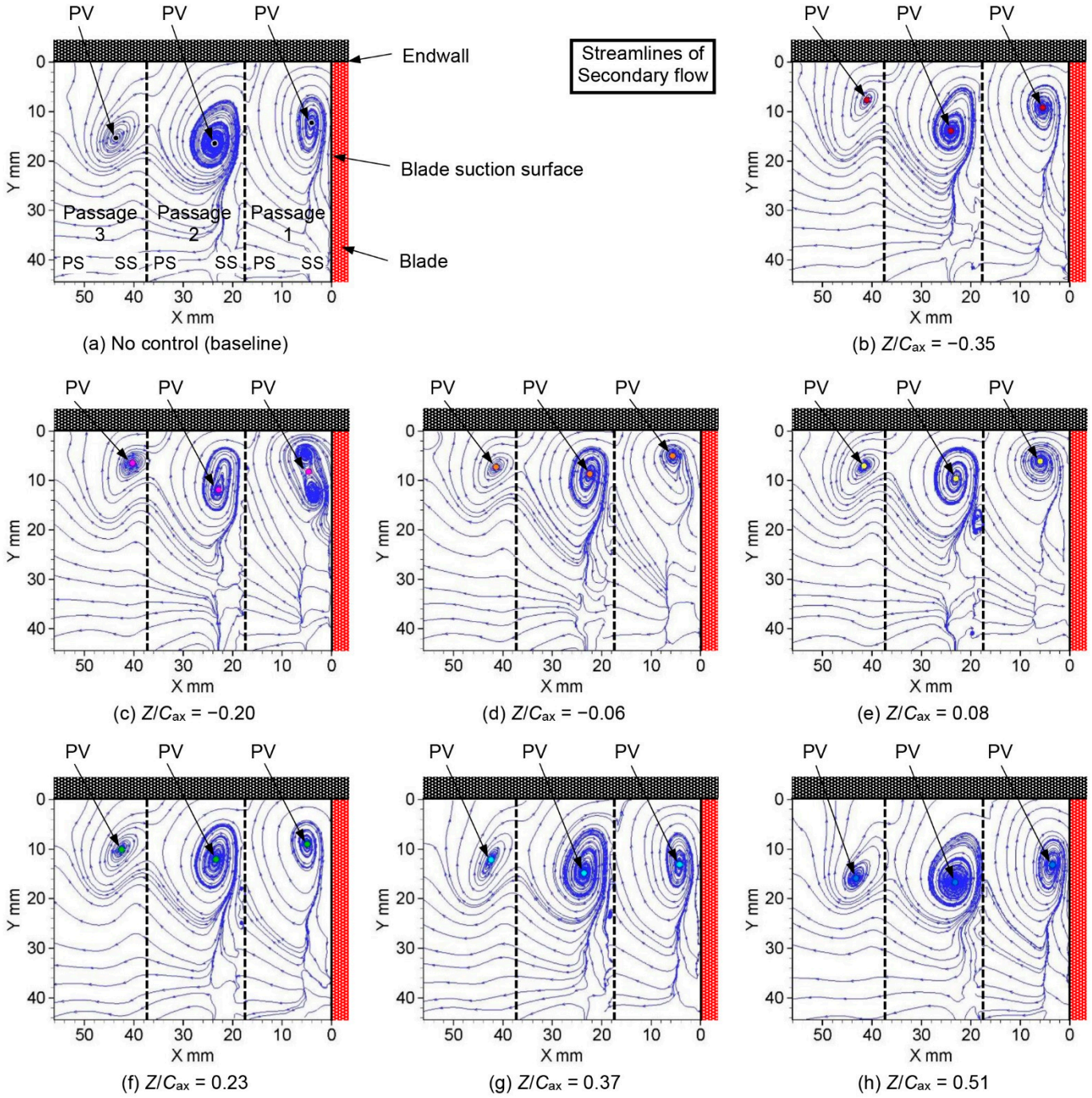

Figure 19. Streamlines of secondary flow at the outlet of the linear turbine cascade at various plasma actuator locations ($Re_{out} = 3.7 \times 10^4$).

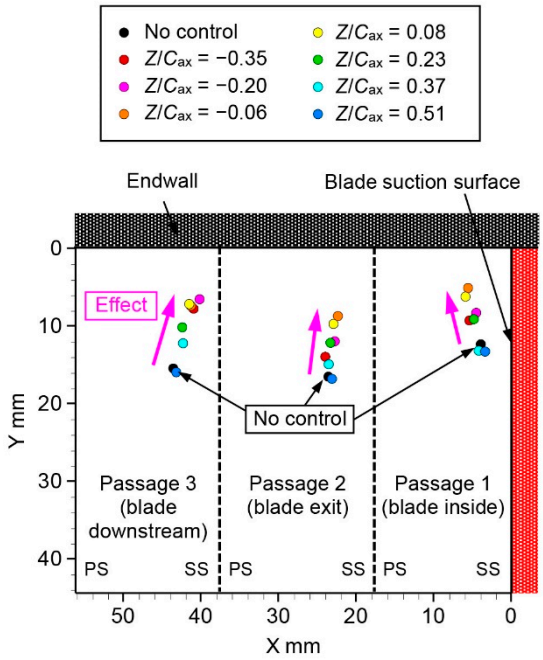

Figure 20. Center positions of passage vortex at various plasma actuator locations ($Re_{out} = 3.7 \times 10^4$).

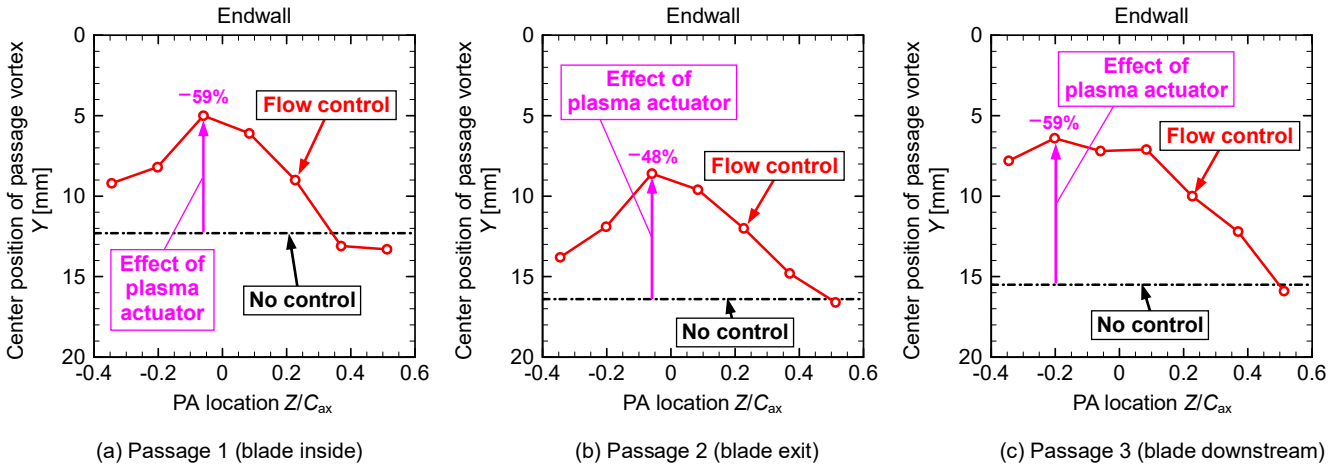

Figure 21. Effect of the plasma actuator location on the center position of the passage vortex ($Re_{out} = 3.7 \times 10^4$).

Figure 22 shows the distribution of turbulence intensities at each actuator location.

Figure 22a shows the turbulence intensity distribution with no control. The turbulence intensity near the center of the passage vortex is high for all three passages. In passage 1, inside the blade, the region with high turbulence intensity (approximately 12%) near the center of the blade suction surface side exists up to approximately $Y = 30$ mm, and this seems to be a result of the influence of the flow separation of the boundary layer on the blade suction surface side. In the turbulence intensity distribution at $Re_{out} = 1.8 \times 10^4$ in Figure 12a, the turbulence intensity of the flow separation region on the blade suction side is approximately 16%. It is considered that the flow separation on the blade suction surface side decreases as the Reynolds number increases.

Figure 22b–h show the measurement results when the plasma actuator is operated. Comparing Figure 22a,b, the peak of the turbulence intensity at the center of the passage vortex shown in Figure 22a with no control disappears in Figure 22b with flow control. Similarly, from Figure 22c–e, there is no peak of turbulence intensity at the center of the passage vortex. The region with high turbulence intensity on the blade suction surface side

in passage 1 extends to around the upward vertical location of Y = 15 mm in the figures. This result indicates that the flow separation region at the blade suction side increases in the blade spanwise direction, due to the suppression effect of the passage vortex. In addition, further downstream, Figure 22f–h show that the turbulence intensity tends to increase, because the suppression effect of the passage vortex weakens.

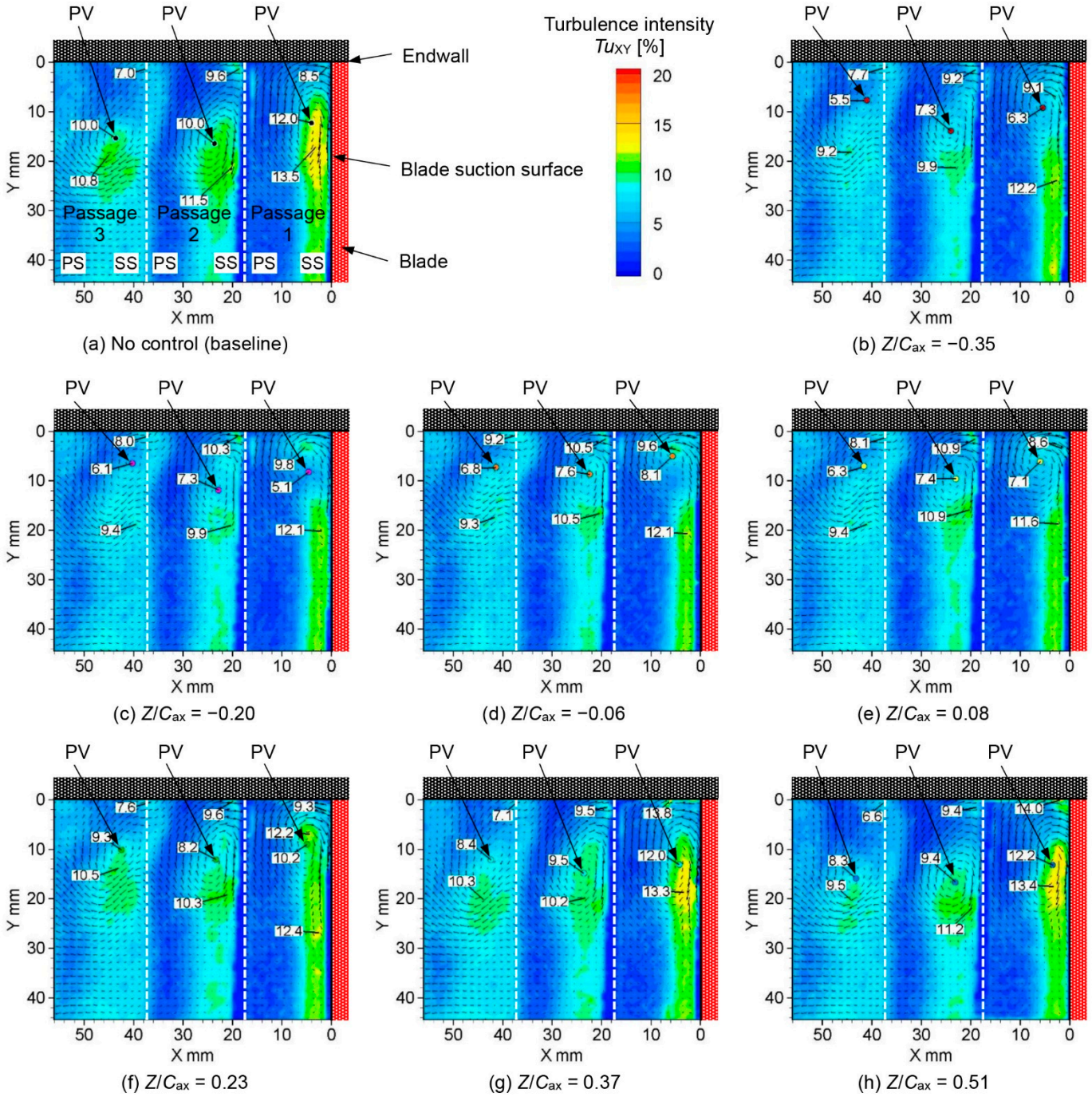

Figure 22. Turbulence intensity distributions of secondary flow at the outlet of the linear turbine cascade at various plasma actuator locations ($Re_{out} = 3.7 \times 10^4$).

Figure 23 shows how the turbulence intensity at the center of the passage vortex of Figure 22 varies depending on the plasma actuator location. In passage 1, shown in Figure 23a, the plasma actuation is effective at Z/C_{ax} = −0.35–0.08, and the turbulence intensity decreases by as much as 58% at Z/C_{ax} = −0.20. The turbulence intensity gradually

increases after Z/C_{ax} = 0.08 and disappears after Z/C_{ax} = 0.37. This tendency is similar to the turbulence intensity distribution at $Re_{out} = 1.8 \times 10^4$ in Figure 13a. In passage 2, shown in Figure 23b, the turbulence intensity is almost constant upstream from Z/C_{ax} = 0.08, and a reduction of 27% in the turbulence intensity is observed. At the furthest downstream position of Z/C_{ax} = 0.51, the turbulence intensity reduction is only 5%. In passage 3, shown in Figure 23c, the turbulence intensity is almost constant at positions further upstream of Z/C_{ax} = 0.08 and decreases by 45% at $Z/C_{ax} = -0.35$. However, the effect of the reduction in turbulence intensity weakens at positions further downstream of Z/C_{ax} = 0.08, and a decrease of only 7% is observed at Z/C_{ax} = 0.23. When Figure 23b,c and Figure 13b,c are compared, Figure 23, with a higher Reynolds number, shows a smaller reduction in turbulence intensity. The reason is that the freestream velocity at $Re_{out} = 3.7 \times 10^4$ is double that at $Re_{out} = 1.8 \times 10^4$. Therefore, the turbulence intensity reduction caused by the induced velocity of the plasma actuator is relatively weakened at higher Re values.

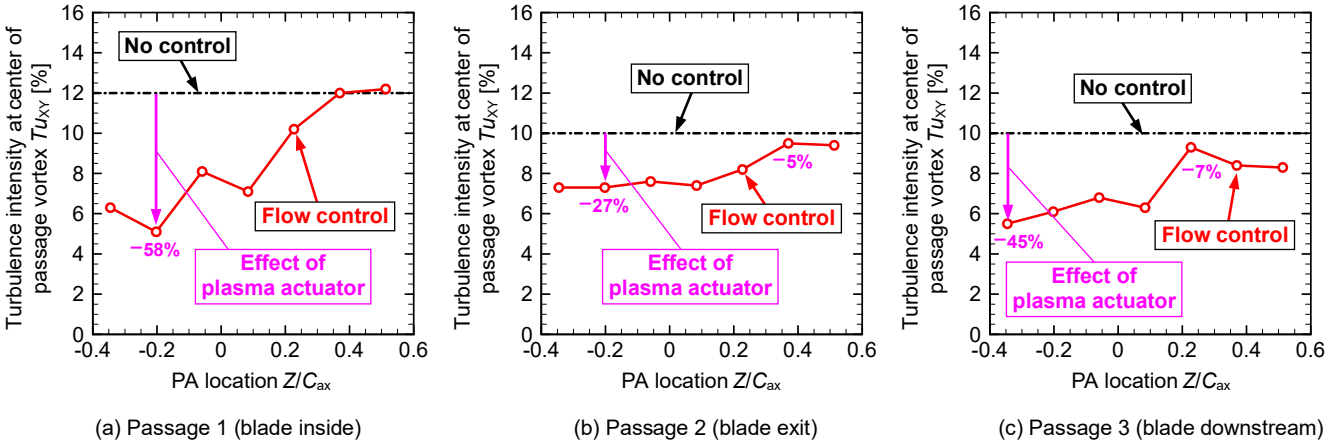

Figure 23. Effect of the plasma actuator location on the turbulence intensity at the center of the passage vortex ($Re_{out} = 3.7 \times 10^4$).

Figure 24 shows the vorticity distribution at each plasma actuator installation location. Because the vorticity is not nondimensionalized, the contour lines are drawn in the two ranges of the lower Re_{out} of 1.8×10^4 shown in Figure 14.

Figure 24a shows the vorticity distribution without control. In all three passages, the absolute value of the vortex is high near the center of the passage vortex, and the peak of the vorticity is gradually weakened as it moves downstream from passage 1 to passage 3, with values of $-1490\ s^{-1}$ at passage 1, $-1100\ s^{-1}$ at passage 2, and $-810\ s^{-1}$ at passage 3.

Figure 24b–h show the measurement results when the plasma actuator is operated. Comparing Figure 24a,b, the regions with a large absolute value of vorticity in Figure 24a with no control are weakened and move towards the upper endwall side in Figure 24b with flow control. Similarly, from Figure 24c–h, the vorticity at the center of the passage vortex becomes weaker. However, at a higher Reynolds number, there is no counterclockwise CV at the blade PS, as is generated in Figure 14 at a lower Reynolds number.

Figure 25 shows how the vortex at the center of the passage vortex of Figure 24 changes with the plasma actuator location. In passage 1, shown in Figure 25a, the effect of reduced absolute vorticity is highest at $Z/C_{ax} = -0.20$, and the vorticity at the center of the passage vortex is weakened by 81%. However, the effect weakens further downstream, and at Z/C_{ax} = 0.23 it shows only a 7% decrease compared to that in the no-control condition. In passage 2, shown in Figure 25b, the tendency changes from that shown in Figure 25a. The vorticity reduction is higher when the plasma actuator is installed inside the blades rather than in the upstream position. This seems to be because the interaction between the passage vortex and upper endwall is weakened, since they are located away from each other when the installation is inside the blades, as observed in Figure 19g, while the passage vortex stays close to the upper endwall surface when the installation is upstream of the blades, as

observed in Figure 19d. In passage 3, shown in Figure 25c, the vortex at the center of the passage vortex is weakened by 55% at $Z/C_{ax} = 0.08$. However, this is a distribution with many variations.

Figure 26 shows the effect of the plasma actuator location on the negative peak value of the vorticity, as shown in Figure 24. In passage 1, shown in Figure 26a, a 28% decrease in the absolute vorticity strength is observed at the furthest upstream position of $Z/C_{ax} = -0.35$. In passage 2, shown in Figure 26b, although there is a variation, only a 21% reduction at $Z/C_{ax} = -0.35$ and a 27% reduction at $Z/C_{ax} = 0.37$ are seen. In passage 3, in Figure 26c, the influence of the location is almost constant, but a decrease of up to 19% is observed at $Z/C_{ax} = 0.08$, which is just downstream of the blade leading edge.

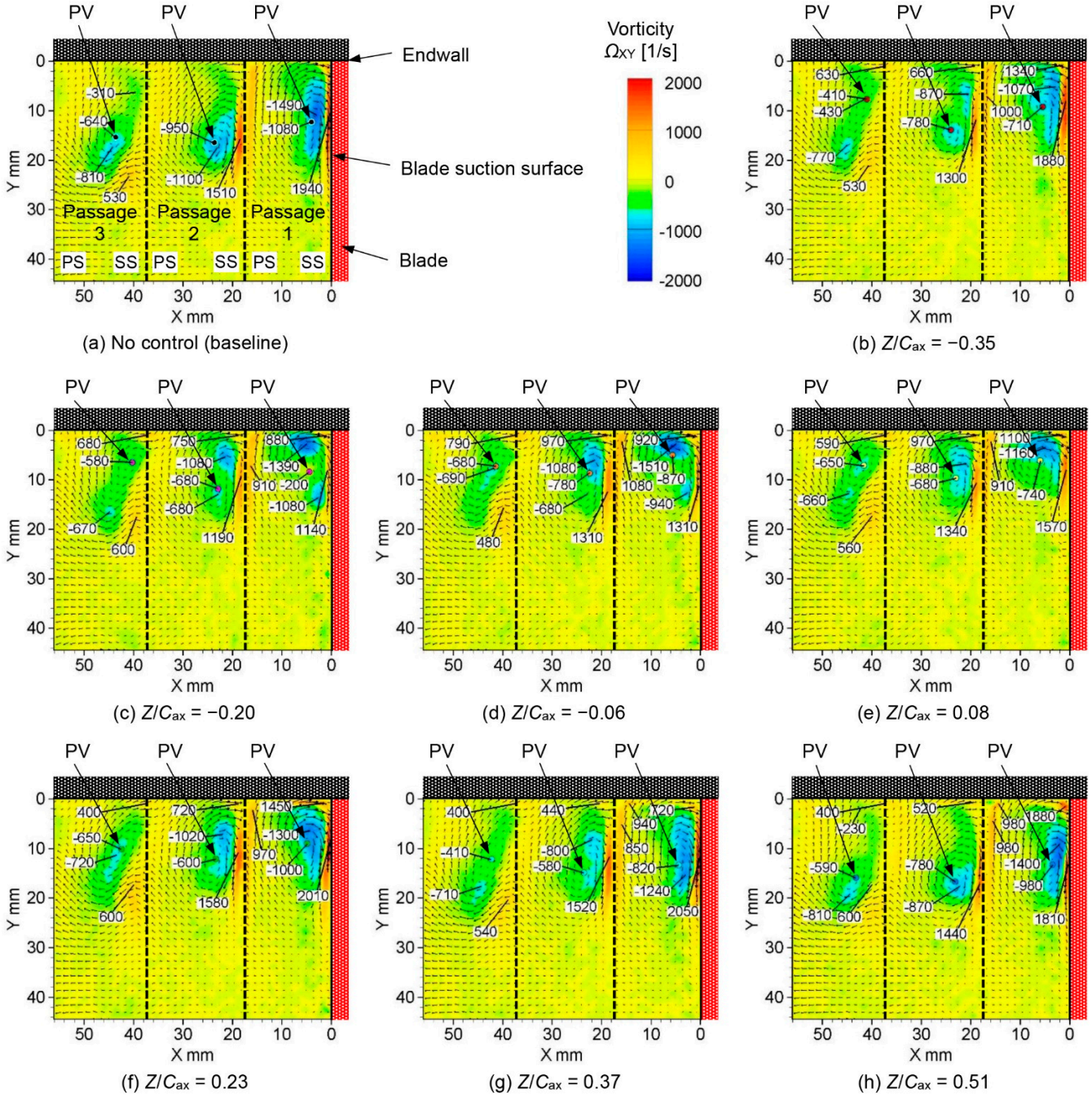

Figure 24. Vorticity distributions of secondary flow at the outlet of the linear turbine cascade at various plasma actuator locations ($Re_{out} = 3.7 \times 10^4$).

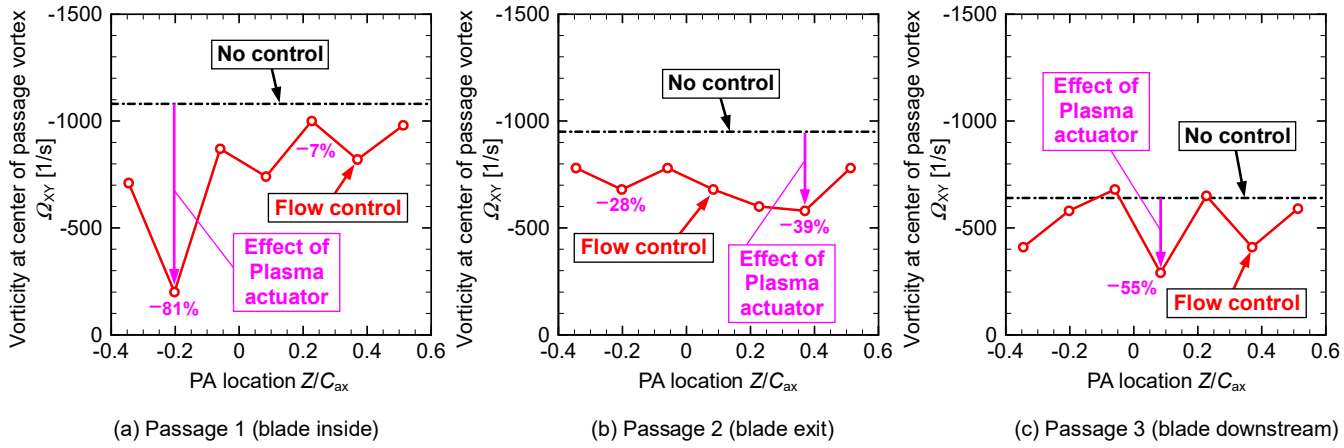

Figure 25. Effect of the plasma actuator location on vorticity at the center of the passage vortex ($Re_{out} = 3.7 \times 10^4$).

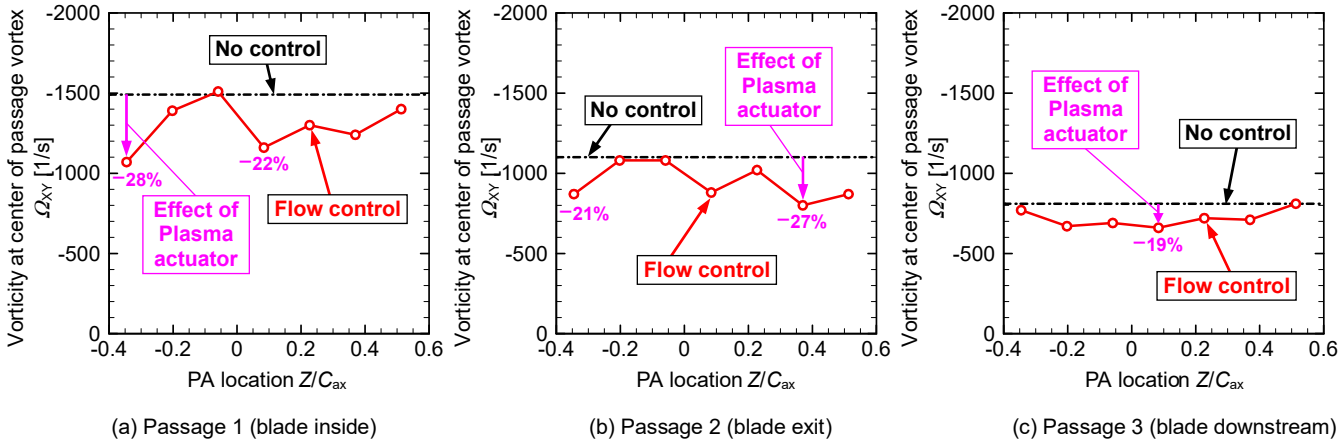

Figure 26. Effect of the plasma actuator location on peak vorticity of the passage vortex ($Re_{out} = 3.7 \times 10^4$).

3.3. Summary of the Location and Percentage of the Maximum Decrease for Each Parameter

Finally, the locations and percentages of the maximum decrease in each parameter at $Re_{out} = 1.8 \times 10^4$ and 3.7×10^4 are summarized in Table 4. Although there were variations in each parameter, the rate of decrease was often maximized at $Z/C_{ax} = -0.20$ and -0.06, and the reduction in the passage vortex was high when the plasma actuator was installed slightly upstream of the blade leading edge. This indicates that it is effective to accelerate the inlet boundary layer with a plasma actuator immediately before it enters the blades. The decrease was often slightly reduced at $Re_{out} = 3.7 \times 10^4$ compared with $Re_{out} = 1.8 \times 10^4$. This is because the freestream velocity is increased at higher Re, and the flow induced by the plasma actuator is decreased.

In previous studies conducted by Zhang et al. [39], the optimal installation location of the plasma actuator for compressor tip leakage vortex control was at 20% of the chord ($Z/C_{ax} = 0.20$). In contrast, the optimal installation locations of the plasma actuator for turbine passage vortex control were at −20% and −6% of the chord ($Z/C_{ax} = -0.20$ and -0.06). This difference in the optimal installation locations is caused by the origin of the vortices. The tip leakage vortex is generated by the leakage flow within the blade, and the passage vortex is generated by the inlet boundary layer of the blade.

Table 4. Summary of the maximum reduction in various parameters.

Reynolds Number Re_{out}	Figure Number	Various Parameters	Passage 1 (Inside)		Passage 2 (Exit)		Passage 3 (Downstream)	
			Position Z/C_{ax}	Reduction Ratio	Position Z/C_{ax}	Reduction Ratio	Position Z/C_{ax}	Reduction Ratio
1.8×10^4	Figure 8	Peak velocity	−0.06	46%	−0.35	63%	−0.35	47%
	Figure 11	PV center position	0.08	39%	0.08	63%	−0.06	71%
	Figure 13	Turbulence intensity	0.08	52%	−0.06	45%	−0.20	56%
	Figure 15	Vorticity at PV center	−0.06	59%	−0.06	71%	−0.35	80%
	Figure 16	Peak vorticity	−0.20	51%	−0.20	62%	−0.35	65%
3.7×10^4	Figure 18	Peak velocity	−0.35	5%	−0.35	20%	−0.20	24%
	Figure 21	PV center position	−0.06	59%	−0.06	48%	−0.20	59%
	Figure 23	Turbulence intensity	−0.20	58%	−0.20	27%	−0.35	45%
	Figure 25	Vorticity at PV center	−0.20	80%	0.37	39%	0.08	55%
	Figure 26	Peak vorticity	−0.35	28%	0.37	27%	0.08	19%

4. Concluding Remarks

In this study, a DBD plasma actuator was applied to reduce the passage vortex of the linear turbine cascade. The passage vortex is a vortex in which the inlet boundary layer from upstream of the turbine hits the leading edge of the turbine blade and rolls up to form a horseshoe vortex, which moves to the suction surface side of the adjacent blade and develops while adding the endwall boundary layer inside the turbine cascade. Using PIV, the two-dimensional velocity distributions of the secondary flow in three passages (inside, at the exit, and downstream of the linear turbine cascade) were measured, and the distributions of the velocity, secondary flow vector, streamlines, turbulence intensity, and vorticity were analyzed. The plasma actuator was located at seven different positions in the range of $Z/C_{ax} = -0.35$–0.51, and the optimum location was determined. Two values of the Reynolds number were also examined, $Re_{out} = 1.8 \times 10^4$ and 3.7×10^4, and the effect of the change in Reynolds number was investigated. The main experimental results were as follows.

(1) The optimum installation location of the plasma actuator was immediately before the leading edge of the blade. This is because the inlet boundary layer can be accelerated before the leading edge weakens the horseshoe vortex, which causes the initial generation of the passage vortex.

(2) Regarding the effect of the Reynolds number, the higher the Re, the weaker the passage vortex suppression effect of the plasma actuator. This is because the freestream velocity increases with an increase in Re; therefore, the induced flow of the plasma actuator becomes relatively weak.

Funding: This research was funded by the Japan Society for the Promotion of Science (JSPS), Grants-in-Aid for Scientific Research (KAKENHI), Grant Number 21K03868.

Data Availability Statement: The data that support the findings of this study are available from the corresponding author upon reasonable request.

Acknowledgments: The author would like to acknowledge Takehiko Segawa of AIST for his support with the PIV experiments.

Conflicts of Interest: The author declares no conflict of interest regarding the publication of this article.

Nomenclature

C	Chord length (mm)
CV	Corner vortex
DBD	Dielectric barrier discharge
H	Blade height (mm)
L	spanwise width of electrodes of plasma actuator (mm)
N	Number of blades
P	Power consumption of plasma actuator
PIV	Particle image velocimetry
PV	Passage vortex
Re	Reynolds number
S	Blade pitch (mm)
T	Time (s)
t	Thickness (mm)
Tu	Turbulence intensity (%)
U	Velocity (m/s)
V	Input voltage (kV)
X	Horizontal coordinate of PIV domain (mm)
Y	Vertical coordinate of PIV domain (mm)
Z	Axial coordinate of turbine cascade (mm)
Greek symbols	
α	Blade angle (°)
Ω	Vorticity component (1/s)
ξ	Blade stagger angle (°)
Subscripts	
ax	Axial
in	Inlet flow
FS	Freestream
out	Outlet flow
PA	Plasma actuator
p-p	Peak to peak
XY	X-Y measurement plane

References

1. Ainley, D.G.; Mathieson, G.C.R. *A Method of Performance Estimation for Axial-Flow Turbines*; British Aeronautical Research Council: London, UK, 1951.
2. Sieverding, C.H. Recent progress in the understanding of basic aspects of secondary flows in turbine blade passages. *ASME J. Eng. Gas Turbines Power* **1985**, *107*, 248–257. [CrossRef]
3. Hourmouziadis, J. Aerodynamic Design of Low Pressure Turbines. In *Blading Design for Axial Turbomachines*; AGARD-LS-167, AGARD Lecture Series No. 167; AGARD: Neue, France, 1989; p. 167.
4. Denton, J.D. Loss mechanisms in turbomachines. *ASME J. Turbomach.* **1993**, *115*, 621–656. [CrossRef]
5. Van Treuren, K.W.; Simon, T.; von Koller, M.; Byerley, A.R.; Baughn, J.W.; Rivir, R. Measurements in a turbine cascade flow under ultra low Reynolds number conditions. *ASME J. Turbomach.* **2002**, *124*, 100–106. [CrossRef]
6. Bons, J.P.; Sondergaard, R.; Rivir, R.B. The fluid dynamics of LPT blade separation using pulsed jets. *ASME J. Turbomach.* **2002**, *124*, 77–85. [CrossRef]
7. Bernardini, C.; Benton, S.I.; Bons, J.P. The effect of acoustic excitation on boundary layer separation of a highly loaded LPT blade. *ASME J. Turbomach.* **2013**, *135*, 051001. [CrossRef]
8. Hodson, H.P.; Howell, R.J. The role of transition in high-lift low-pressure turbines for aeroengines. *Prog. Aerosp. Sci.* **2005**, *41*, 419–454. [CrossRef]
9. Schobeiri, M.T.; Öztürk, B.; Ashpis, D.E. Effect of Reynolds number and periodic unsteady wake flow condition on boundary layer development, separation, and intermittency behavior along the suction surface of a low pressure turbine blade. *ASME J. Turbomach.* **2007**, *129*, 92–107. [CrossRef]

10. Sanders, D.D.; O'Brien, W.F.; Sondergaard, R.; Polanka, M.D.; Rabe, D.C. Predicting separation and transitional flow in turbine blades at low Reynolds numbers—Part I: Development of prediction methodology. *ASME J. Turbomach.* **2011**, *133*, 031011. [CrossRef]
11. Sanders, D.D.; O'Brien, W.F.; Sondergaard, R.; Polanka, M.D.; Rabe, D.C. Predicting separation and transitional flow in turbine blades at low Reynolds numbers—Part II: The application to a highly separated turbine blade cascade geometry. *ASME J. Turbomach.* **2011**, *133*, 031012. [CrossRef]
12. Wang, X.; Liang, L.; Kang, S. Numerical simulations on flow separation within an axial turbine at very low Reynolds number. In Proceedings of the ASME Turbo Expo 2015: Turbine Technical Conference and Exposition, Montreal, QC, Canada, 15–19 June 2015; ASME Turbo Expo: Montreal, QC, Canada, 12 August 2015. [CrossRef]
13. Mittal, R.; Venkatasubramanian, S.; Najjar, F. Large-eddy simulation of flow through a low-pressure turbine cascade. In Proceedings of the 15th AIAA Computational Fluid Dynamics Conference, Anaheim, CA, USA, 11–14 June 2001. [CrossRef]
14. Sharma, O. Impact of Reynolds number on LP turbine performance. In *Minnnowbrook II Workshop on Boundary Layer Transition in Turbomachines*; NASA/CP-1998-206958; NASA Technical Reports Server: Sunnyvale, CA, USA, 1998; pp. 65–69. Available online: https://ntrs.nasa.gov/citations/19980206205 (accessed on 1 March 2022).
15. Rivir, R.B.; Sondergaard, R.; Bons, J.P. Control of Separation in Turbine Boundary Layers. In Proceedings of the 2nd AIAA Flow Control Conference, Oregon, Portland, 28 June–1 July 2004. [CrossRef]
16. Bons, J.; Benton, S.; Bernardini, C.; Bloxham, M. Active flow control for low-pressure turbines. *AIAA J.* **2018**, *56*, 2687–2698. [CrossRef]
17. Huang, J.; Corke, T.; Thomas, F. Plasma Actuators for separation control of low pressure turbine blades. In Proceedings of the 41st Aerospace Sciences Meeting and Exhibit, Reno, Nevada, 6–9 January 2003. [CrossRef]
18. Hultgren, L.; Ashpis, D. Demonstration of separation delay with glow discharge plasma actuators. In Proceedings of the 41st Aerospace Sciences Meeting and Exhibit, Reno, Nevada, 6–9 January 2003. [CrossRef]
19. List, J.; Byerley, A.; McLaughlin, T.; Dyken, R.V. Using a plasma actuator to control laminar separation on a linear cascade turbine blade. In Proceedings of the 41st Aerospace Sciences Meeting and Exhibit, Reno, Nevada, 6–9 January 2003. [CrossRef]
20. Huang, J. Separation Control over Low Pressure Turbine Blades Using Plasma Actuators. Dissertation, The University of Notre Dame, Notre Dame, IN, USA, 2005; p. 56. Available online: https://www3.nd.edu/~{}tcorke/Huang_Thesis.pdf?msclkid=53e3f6f1b71611ec8a1240b51436b2b9 (accessed on 1 March 2022).
21. Boxx, I.G.; Newcamp, J.M.; Franke, M.E.; Woods, N.M.; Rivir, R.B. A PIV Study of a plasma discharge flow-control actuator on a flat plate in an aggressive pressure induced separation. In Proceedings of the ASME Turbo Expo 2006: Power for Land, Sea, and Air, Barcelona, Spain, 8–11 May 2006; Volume 3, pp. 1231–1242. [CrossRef]
22. Pescini, E.; Marra, F.; De Giorgi, M.G.; Francioso, L.; Ficarella, A. Investigation of the boundary layer characteristics for assessing the DBD plasma actuator control of the separated flow at low Reynolds numbers. *Exp. Therm. Fluid Sci.* **2017**, *81*, 482–498. [CrossRef]
23. Pescini, E.; De Giorgi, M.G.; Suma, A.; Francioso, L.; Ficarella, A. Separation control by a microfabricated SDBD plasma actuator for small engine turbine applications: Influence of the excitation waveform. *Aerosp. Sci. Technol.* **2018**, *76*, 442–454. [CrossRef]
24. Zhou, C.; Hodson, H.; Tibbott, I.; Stokes, M. Effects of Winglet Geometry on the Aerodynamic Performance of Tip Leakage Flow in a Turbine Cascade. *Trans. ASME J. Turbomach.* **2013**, *135*, 051009. [CrossRef]
25. Coull, J.D.; Atkins, N.R.; Hodson, H.P. High Efficiency Cavity Winglets for High Pressure Turbines. In Proceedings of the ASME Turbo Expo 2014: Turbine Technical Conference and Exposition, Düsseldorf, Germany, 16–20 June 2014. [CrossRef]
26. Volino, R.J. Control of Tip Leakage in A High Pressure Turbine Cascade Using Tip Blowing. In Proceedings of the ASME Turbo Expo 2016: Turbomachinery Technical Conference and Exposition, Seoul, Korea, 13–17 June 2016. [CrossRef]
27. Van Ness II, D.K.; Corke, T.C.; Morris, S.C. Turbine Tip Clearance Flow Control Using Plasma Actuator. In Proceedings of the 44th AIAA Aerospace Sciences Meeting and Exhibit, Reno, Nevada, 9–12 January 2006. [CrossRef]
28. Matsunuma, T.; Segawa, T. Tip leakage flow reduction of a linear turbine cascade using string-type DBD plasma actuators. In Proceedings of the ASME Turbo Expo 2018: Turbomachinery Technical Conference and Exposition, Oslo, Norway, 11–15 June 2018; Volume 2B. [CrossRef]
29. Yu, J.; Lu, Y.; Wang, Y.; Chen, F.; Song, Y. Experimental study on the plasma actuators for the tip leakage flow control in a turbine cascade. *Aerosp. Sci. Technol.* **2022**, *121*, 107195. [CrossRef]
30. Schmid, J.; Schulz, A.; Bauer, H.J. Influence of a non-axisymmetric endwall on the flow field in a turbine passage—High resolution LDV. In Proceedings of the ASME Turbo Expo 2018, Oslo, Norway, 11–15 June 2018. [CrossRef]
31. Sangston, K.; Little, J.; Lyall, M.E.; Sondergaard, R. End wall loss reduction of high lift low pressure turbine airfoils using profile contouring—Part 2: Validation. *ASME J. Turbomach.* **2014**, *136*, 081006. [CrossRef]
32. Chung, J.T.; Simon, T.W.; Buddhavarapu, J. Three-dimensional flow near the blade/endwall junction of a gas turbine: Application of a boundary layer fence. In Proceedings of the ASME Turbo Expo 1991, Orland, FL, USA, 3–6 June 1991. [CrossRef]
33. Shyam, V.; Ameri, A.; Poinsatte, P.; Thurman, D.; Wroblewski, A.; Snyder, C. Application of pinniped vibrissae to aeropropulsion. In Proceedings of the ASME Turbo Expo 2015, Montréal, QC, Canada, 15–19 June 2015. [CrossRef]
34. Bloxham, M.J.; Bons, J.P. A global approach to turbomachinery flow control: Passage vortex control. *Trans. ASME J. Turbomach.* **2014**, *136*, 041003. [CrossRef]

35. Benton, S.I.; Bons, J.P.; Sondergaard, R. Secondary flow loss reduction through blowing for a high-lift front-loaded low pressure turbine cascade. *Trans. ASME J. Turbomach.* **2013**, *135*, 021020. [CrossRef]
36. Benton, S.I.; Bernardini, C.; Bons, J.P.; Sondergaard, R. Parametric optimization of unsteady end wall blowing on a highly loaded low-pressure turbine. *Trans. ASME J. Turbomach.* **2014**, *136*, 071013. [CrossRef]
37. Matsunuma, T.; Segawa, T. Effects of input voltage and freestream velocity on active flow control of passage vortex in a linear turbine cascade using dielectric barrier discharge plasma actuator. *Energies* **2020**, *13*, 764. [CrossRef]
38. De Giorgi, M.G.; Pescini, E.; Marra, F.; Ficarella, A. Plasma actuator scaling down to improve its energy conversion efficiency for active flow control in modern turbojet engines compressors. *Appl. Therm. Eng.* **2016**, *106*, 334–350. [CrossRef]
39. Zhang, H.; Wu, Y.; Li, Y.; Yu, X.; Liu, B. Control of compressor tip leakage flow using plasma actuation. *Aerosp. Sci. Technol.* **2019**, *86*, 244–255. [CrossRef]
40. Saddoughi, S.; Bennett, G.; Boespflug, M.; Puterbaugh, S.L.; Wadia, A.R. Experimental investigation of tip clearance flow in a transonic compressor with and without plasma actuators. In Proceedings of the ASME Turbo Expo 2014: Turbine Technical Conference and Exposition, Düsseldorf, Germany, 16–20 June 2014; Volume 2A. [CrossRef]
41. Sharma, O.P.; Butler, T.L. Predictions of endwall losses and secondary flows in axial flow turbine cascades. *Trans. ASME J. Turbomach.* **1987**, *109*, 229–236. [CrossRef]
42. Roth, J.R.; Sherman, D.M.; Wilkinson, S.P. Boundary layer flow control with a one atmosphere uniform grow discharge. In Proceedings of the 36th AIAA Aerospace Sciences Meeting and Exhibit, Reno, NV, USA, 12–15 January 1998. [CrossRef]
43. Corke, T.C.; Post, M.L.; Orlov, D.M. SDBD plasma enhanced aerodynamics: Concepts, optimization and applications. *Prog. Aerosp. Sci.* **2007**, *43*, 193–217. [CrossRef]
44. Corke, T.C.; Enloe, C.L.; Wilkinson, S.P. Dielectric barrier discharge plasma actuators for flow control. *Annu. Rev. Fluid Mech.* **2010**, *42*, 505–529. [CrossRef]
45. Wang, J.J.; Choi, K.S.; Feng, L.H.; Jukes, T.N.; Whalley, R.D. Recent developments in DBD plasma flow control. *Prog. Aerosp. Sci.* **2013**, *62*, 52–78. [CrossRef]
46. Matsunuma, T. Unsteady flow field of an axial-flow turbine rotor at a low Reynolds number. *Trans. ASME J. Turbomach.* **2007**, *129*, 360–371. [CrossRef]
47. Ashpis, D.E.; Thurman, D.R. *DBD Plasma Actuators for Flow Control in Air Vehicles and Jet Engines—Simulation of Flight Conditions in Test Chambers by Density Matching*; TM-2011-217006; NASA: Washington, DC, USA, 2011. Available online: https://ntrs.nasa.gov/api/citations/20110008545/downloads/20110008545.pdf (accessed on 1 March 2022).
48. Valerioti, J.A.; Corke, T.C. Pressure dependence of dielectric barrier discharge plasma flow actuators. *AIAA J.* **2012**, *50*, 1490–1502. [CrossRef]